Available online at www.sciencedirect.com
SCIENCE DIRECT®
OCEAN ENGINEERING
ELSEVIER
Ocean Engineering XX (2004) XXX–XXX
www.elsevier.com/locate/oceaneng

Optimal identification of potential-radiation hydrodynamics for moored floating structures—a new general approach in state space

Mario A. Jordán *, Reinel Beltrán-Aguedo

Dto. de Ingeniería Eléctrica, Universidad Nacional del Sur, Av. Alem 1253, 8000 Bahía Blanca, Argentina

Received 27 August 2003; accepted 6 January 2004

Abstract

In this paper, a new state-space model of the potential-radiation hydrodynamics in moored ocean engineering floating structures and its parameter identification are presented. The raw data for this goal are the added mass and potential-damping matrices in frequency-discrete domain.

In a preliminary study of existing approaches in the literature, two mathematical models and their estimation are comparatively analysed in detail. These served in the development of the new approach that shares certain main advantages of the previous approaches.

The model is identified in a least-squares sense using a weighted norm and a free control parameter to accomplish a trade-off between quality and stability. This reduces numerical instability problems and also keeps the analytical and computational benefits of a parametric state-space model. The model can be conveniently expressed in any usual canonical form in state space.

The application of the model acceptably accurate reproduces the behaviour of the potential-radiation hydrodynamic forces in time. Case studies involving a semisubmersible and buoys are shown to demonstrate the features of the proposed approach.

Keywords: Potential-radiation hydrodynamics; Moored floating structures; Convolution model; State-space model; Parameter estimation

* Corresponding author. Tel.: +54-291-4595100x3310; fax: +54-291-4595154.
E-mail address: mjordan@criba.edu.ar (M.A. Jordán).

0029-8018/$ - see front matter © 2004 Published by Elsevier Ltd.
doi:10.1016/j.oceaneng.2004.01.007

1. Introduction

Moored floating structures are employed in a gamut of marine operations that involve basically transport, towing, launching and submergence of offshore units and components. This class of ocean engineering systems (OE systems) mainly includes platforms, buoys, barges, crane ships, pipe-lying ships and drill ships. Often these structures behave in complex forms due to nonlinearity in their dynamics, and for a monochromatic wave excitation, it causes unpredictable evolutions even for normal operation. These situations call for a need of feedback control. Usual controls for draught, roll stabilisation, dynamic positioning and control of nonlinear oscillations require detailed dynamic models for reaching high-quality performance (Youssef et al., 2002; Gawad et al., 2001; Fajinmi and Brown, 1999; Fossen, 1999; Aamo and Fossen, 1999). Also stability analysis of nonlinear dynamics demands parameterised models in order to apply modern mathematical tools (Kreuzer et al., 2002; Gottlieb and Yim, 1993; Umar and Datta, 2003; Gottlieb and Yim, 1997; Kim and Bernitsas, 2001).

The dynamics of an OE system is established as a balanced among, on one side, inertia, Coriolis and centrifugal forces, and on the other side, restoring, hydrodynamic and propulsion forces. Hydrodynamics is an important part of the whole model, and hence it is required to be precisely described for achieving the above-mentioned control goals.

The modelling of the hydrodynamics is in general complex and is basically obtained from numerical Finite Element Methods using the Flow Potential Theory of Airy or the nonlinear Theory of Navier–Stokes.

From the point of view of the hydrodynamics, an OE system interacts with the fluid environment due to its self-motion. This interaction is subject to incident, refraction and radiation-induced forces. In particular, the last forces are caused from the velocity and acceleration of the OE system structure with a memory effect with vanishes in time. This hydrodynamics is highly dependent on the hull geometry and can be characterised by time-weighting functions or more elaborated parameterised models.

In the literature there exist two approaches for characterising the radiation hydrodynamics in time domain: convolution description (Cummins, 1962; Ogilvie, 1964), and state-space representation (Jiang, 1991; Schelin et al., 1993).

The start point within Airy's theory for both approaches are the so-called hydrodynamic coefficients, added mass and potential damping, which represent the radiation-induced hydrodynamics in frequency domain. These are experimentally calculated employing test facilities (shakers) (Wu and Hsieh, 2001; Chakrabarti, 1994), or by means of ad hoc programs that simulate hydrodynamic loads for different monochromatic oscillations in a prespecified range of frequencies (Soylemez and Atlar, 2000).

It is not clear enough in the literature which one of the two both mentioned approaches is more adequate for stability analysis and controller design. In this paper, both mathematical formalisms are explored from the viewpoint of the representation and identification. On the basis of comparative properties of both

descriptions, a new state-space model is developed, which shares advantages of the previous ones. The development of the new model and its identification is quite general, embracing all the OE system structures mentioned at the beginning.

The paper is organised as follows. First, the dynamics of a generic OE system is explained. Therein, the hydrodynamics is focused on Airy's theory framework. Afterwards modelling and identification methods for the existing approaches are described from a new perspective. An extensive comparative study of their properties gives rise to the new approach in state space. Next, an optimal parameter estimation of this model is proposed. Finally, case studies are designed to test and show features of the new approach.

2. Dynamics of an OE system

An OE system possesses a dynamics expressed by the solution of the ODE

$$M(\mathbf{q})\ddot{\mathbf{q}} + \mathbf{K}(\mathbf{q}, \dot{\mathbf{q}}) = \mathbf{F}_S(\mathbf{q}, \dot{\mathbf{q}}) + \mathbf{F}_R(\dot{\mathbf{q}}, \ddot{\mathbf{q}}, \mathbf{s}_0), \tag{1}$$

where M is the generalised inertia matrix, $\mathbf{K}$ the Coriolis and centrifugal generalised forces, $\mathbf{F}_S$ the resultant of restoring forces (buoyancy, weight and mooring-lines forces), thruster, propel, incident, diffraction and viscous forces), $\mathbf{F}_R$ the radiation force matter of this analysis, $\mathbf{q}$, $\dot{\mathbf{q}}$ and $\ddot{\mathbf{q}}$ are the generalised position, velocity and acceleration vectors of the fixed reference system centre O, respectively (see Fig. 1), and finally $\mathbf{s}_0$ is the so-called regular part of the hydrodynamic radiation force.

The generalised position vector is

$$\mathbf{q} = [\,x \quad y \quad z \quad \varphi \quad \theta \quad \psi\,]^{\mathrm{T}}, \tag{2}$$

with the modes x (surge), y (sway), z (heave), φ (roll), θ (pitch) and ψ (yaw).

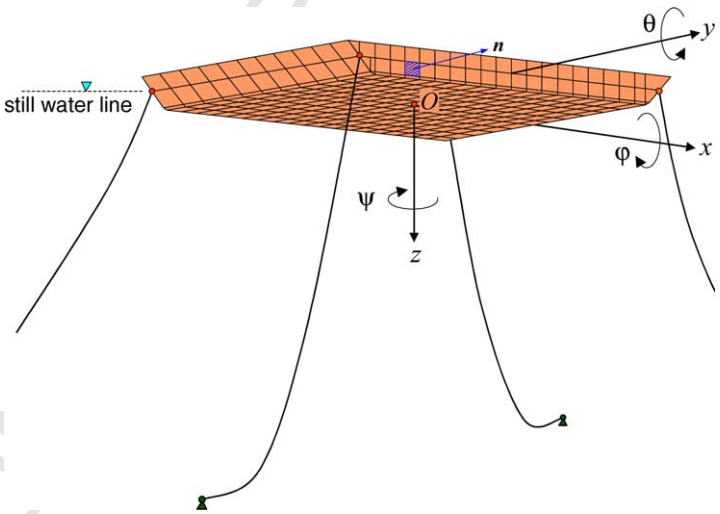

Fig. 1. Coordinate frame for a moored OE system barge.

Positive displacements and positive counterclockwise rotations are subject to the convention depicted in Fig. 1. The centre O is assumed to be the material point where the sensors (gyroscope, accelerometers, inclinometers) are placed for capturing the OE system behaviour. The notation used for matrices, variables and constants is in italic, while those of vectors in bold. In addition, a dot over a symbol represents differentiation with respect to time.

3. Hydrodynamics of an OE system

The hydrodynamics of an OE system describes the interaction of the moving structure with the surrounding fluid. It depends on the geometric characteristics of the structure wet part, and also of direction and frequency of incident waves. The hydrodynamics encompasses the radiation, diffraction and incident forces. All these can be explained by means of the Potential Flow Theory. For irrotational fluid, the potential flow function Φ (x, y, z) satisfies the Laplace equation (Dean and Dalrymple, 1991)

$$\nabla^2\Phi(x,y,z) = 0. \tag{3}$$

This equation must be solved under some boundary conditions imposed for the free surface, the structure hull and the depth.

The potential flow at any geometric point (x, y, z) of the wet hull is the result of three phenomena: the movement of the incoming wave, the perturbation of the body that diffracts the incident wave, and finally the radiation induced by the moving body. All these phenomena act simultaneously. For small steepness of the incident wave (say for $H/\lambda < 1/50$, with H the wave span and λ the wave length) and unsteady small-enough body motions, the potential flow can be expressed as

$$\Phi(x,y,z,t) = \Phi_{\mathrm{I}} + \Phi_{\mathrm{D}} + \sum_j \Phi_{\mathrm{R}_j}, \tag{4}$$

with $j \in \{x, y, z, \varphi, \theta, \psi\}$, Φ_{I}, Φ_{D} and Φ_{R} the incident, diffracted and radiated potentials due to the unsteady motion in the modes j, respectively.

To find functions Φ_{D} and Φ_{R} that satisfy (3), the Bernoulli equation is invoked leading to the free boundary conditions

$$\frac{\partial^2\Phi_{\mathrm{D}}}{\partial t^2} + g\frac{\partial\Phi_{\mathrm{D}}}{\partial z} = 0 \tag{5}$$

$$\frac{\partial^2\Phi_{\mathrm{R}_j}}{\partial t^2} + g\frac{\partial\Phi_{\mathrm{R}_j}}{\partial z} = 0. \tag{6}$$

Additionally, the kinematic hull boundary conditions are

$$\frac{\partial\Phi_{\mathrm{D}}}{\partial\mathbf{n}} = -\frac{\partial\Phi_{\mathrm{I}}}{\partial\mathbf{n}}, \quad \text{on } S_0 \tag{7}$$

$$\frac{\partial\Phi_{\mathrm{R}_j}}{\partial\mathbf{n}} = \dot{\boldsymbol{q}}_i\mathbf{n}_i, \quad \text{on } S_0. \tag{8}$$

where S_0 is the wet hull surface at hydrostatic equilibrium, $\mathbf{n}$ the normal at the considered hull point and $\mathbf{n}_i$ a versor for the motion $\dot{q}_i \in \{\dot{x}, \dot{y}, \dot{z}, \dot{\varphi}, \dot{\theta}, \dot{\psi}\}$ (see Fig. 1).

Finally, at infinitely distant positions the potentials Φ_D and Φ_R accomplish

$$\lim_{\sqrt{x^2+y^2+z^2}\to\infty} \nabla\Phi_D = \lim_{\sqrt{x^2+y^2+z^2}\to\infty} \nabla\Phi_{R_j} = 0. \tag{9}$$

The linearised Bernoulli equation holds

$$\frac{p_h - p_a}{\rho} = \frac{\partial\Phi}{\partial t} + gz, \tag{10}$$

with p_a and p_h the atmospheric and the fluid pressure, respectively, which gives the load on the hull by means of the integration over S_0

$$F_j(x,y,z,t) = -\rho\int_{S_0} \frac{\partial\Phi_I}{\partial t}\,\mathrm{d}\mathbf{s} - \rho\int_{S_0} \frac{\partial\Phi_D}{\partial t}\,\mathrm{d}\mathbf{s} - \rho\sum_j \int_{S_0} \frac{\partial\Phi_{R_j}}{\partial t}\,\mathrm{d}\mathbf{s} - \rho g\int_{S_0} z\,\mathrm{d}\mathbf{s}, \tag{11}$$

with d$\mathbf{s}$ being an elemental hull surface with normal $\mathbf{n}$. The first, second and third terms in (11) represent the incident, diffraction and radiation forces, respectively. The last term in (11) characterises the hydrostatic forces.

Following Cummins (1962) and Ogilvie (1964) the radiation potential is represented by

$$\Phi_{R_j}(x,y,z,t) = \mathbf{c}_i^T(x,y,z)\dot{\mathbf{q}}(x,y,z,t) + \int_{-\infty}^{t}\sum_j \kappa_{ij}(x,y,z,t-\tau)\dot{q}_j(x,y,z,t)\,\mathrm{d}\tau, \tag{12}$$

with $\dot{\mathbf{q}}$ and $\dot{q}_j$ the velocity vector and component of the hull point (x, y, z), $\mathbf{c}_i$ a point-dependent constant vector and κ_{ij} a point-dependent memory function representing the past history of the fluid motion in the coupled modes ij after a sudden change of position of the body.

3.1. Radiation hydrodynamics in time domain

Introducing (12) in the third term of (11) and performing the integral on the wet hull causes the radiation-induced hydrodynamic force acting upon the body

$$\mathbf{F}_R(t) = -M_\infty\ddot{\mathbf{q}}(t) - \int_{-\infty}^{t} K(t-\tau)\dot{\mathbf{q}}(\tau)\,\mathrm{d}\tau \tag{13}$$

$$\mathbf{F}_R(t) = -M_\infty\ddot{\mathbf{q}}(t) - \int_{0}^{t} K(\tau)\dot{\mathbf{q}}(t-\tau)\,\mathrm{d}\tau, \tag{14}$$

where the matrix M_∞ is the value of the so-called added mass at an infinitely large frequency and $K(\tau)$ is a functional matrix of the independent variable τ containing all the memory of the fluid response. It depends only on the geometry of the wet

part of the submersed body. It is noticeable that the evolution in time of $\mathbf{F}_R$ depends on the acceleration and velocity of the point O at time t, as well as on the past history of velocity of O, which is weighted through the characteristic matrix function $K(\tau)$ on $\tau \in [0, \infty]$.

3.2. Radiation hydrodynamics in frequency domain

Consider the fluid-structure system at rest and an impulsive excitation vector $\dot{\mathbf{q}}(\tau) = -[\delta(\tau), \ldots, \delta(\tau)]^T$, where δ is the Dirac impulsive function. Then from (13) or (14), a radiation-included hydrodynamic force $\mathbf{F}_{R_\delta}(t)$ occurs, whose evolution in time is absolutely integrable in $t \in [0, \infty]$. Hence, using the Fourier transform in it, results in

$$\mathscr{F}\{\mathbf{F}_{R_\delta}(t)\} = -D(\omega) - j\omega M_a(\omega), \tag{15}$$

with $j = \sqrt{-1}$, $M_a(\omega)$ and $D(\omega)$ the added-mass and potential-damping matrices, respectively. For a general absolutely time-integrable velocity $\dot{\mathbf{q}}$, the force in frequency domain results

$$\mathbf{F}_R(j\omega) = (-D(\omega) - j\omega M_a(\omega))\dot{\mathbf{q}}(j\omega) \tag{16}$$

$$\mathbf{F}_R(j\omega) = -D(\omega)\dot{\mathbf{q}}(j\omega) - M_a(\omega)\ddot{\mathbf{q}}(j\omega). \tag{17}$$

Besides, the asymptotic properties are valid

$$\lim_{\omega\to\infty} M_a(\omega) = M_\infty \neq 0 \tag{18}$$

$$\lim_{\omega\to\infty} D(\omega) = D_\infty = 0. \tag{19}$$

The matrices $M_a(\omega)$ and $D(\omega)$ are numerically calculated for each frequency using Finite Element Methods and Strip Theory. An ad hoc program for this divides the wet hull into strips and computes the complex relation $F_{R_j}(j\omega)/\dot{q}_k(j\omega)$ for every strip so that matrix elements d_{jk} and $m_{a_{jk}}$ can be integrated over S_0 as

$$d_{jk}(\omega) = -\int_{S_0} \mathrm{Re}\left\{\frac{F_{R_j}(j\omega)}{\dot{q}_k(j\omega)}\right\} d\mathbf{s} \tag{20}$$

$$m_{a_{jk}}(\omega) = -\frac{1}{\omega}\int_{S_0} \mathrm{Im}\left\{\frac{F_{R_j}(j\omega)}{\dot{q}_k(j\omega)}\right\} d\mathbf{s}, \tag{21}$$

with point-dependent $(\dot{q}_k)_{\mathbf{ds}} \in \{\dot{x}, \dot{y}, \dot{z}, \dot{\varphi}, \dot{\theta}, \dot{\psi}\}$, $(F_{R_j})_{\mathbf{ds}}$ the point-dependent element i of $\mathbf{F}_R$, and $\mathbf{ds}$ an elemental strip normal vector for an induced monochromatic motion of frequency ω.

The matrices M_a and D are symmetric; however, their elements $m_{a_{jk}}(\omega)$ and $d_{jk}(\omega)$ are symmetric and skew-symmetric, respectively. They can be simplified by exploiting different common body symmetries of OE systems, for instance: port/starboard, fore/aft, bottom–top and combination of them (Fossen, 1994). For instance:

1. Port/starboard symmetry

$$M_a = \begin{bmatrix} m_{a_{11}} & 0 & m_{a_{13}} & 0 & m_{a_{15}} & 0 \\ 0 & m_{a_{22}} & 0 & m_{a_{24}} & 0 & m_{a_{26}} \\ m_{a_{13}} & 0 & m_{a_{33}} & 0 & m_{a_{35}} & 0 \\ 0 & m_{a_{24}} & 0 & m_{a_{44}} & 0 & m_{a_{46}} \\ m_{a_{15}} & 0 & m_{a_{35}} & 0 & m_{a_{55}} & 0 \\ 0 & m_{a_{26}} & 0 & m_{a_{46}} & 0 & m_{a_{66}} \end{bmatrix} \quad (22)$$

2. Fore/aft symmetry

$$M_a = \begin{bmatrix} m_{a_{11}} & 0 & 0 & 0 & m_{a_{15}} & m_{a_{16}} \\ 0 & m_{a_{22}} & m_{a_{23}} & m_{a_{24}} & 0 & 0 \\ 0 & m_{a_{23}} & m_{a_{33}} & m_{a_{34}} & 0 & 0 \\ 0 & m_{a_{24}} & m_{a_{34}} & m_{a_{44}} & 0 & 0 \\ m_{a_{15}} & 0 & 0 & 0 & m_{a_{55}} & m_{a_{56}} \\ m_{a_{16}} & 0 & 0 & 0 & m_{a_{56}} & m_{a_{66}} \end{bmatrix} \quad (23)$$

3. Port/starboard and fore/aft symmetries

$$M_a = \begin{bmatrix} m_{a_{11}} & 0 & 0 & 0 & m_{a_{15}} & 0 \\ 0 & m_{a_{22}} & 0 & m_{a_{24}} & 0 & 0 \\ 0 & 0 & m_{a_{33}} & 0 & 0 & 0 \\ 0 & m_{a_{24}} & 0 & m_{a_{44}} & 0 & 0 \\ m_{a_{15}} & 0 & 0 & 0 & m_{a_{55}} & 0 \\ 0 & 0 & 0 & 0 & 0 & m_{a_{66}} \end{bmatrix} \quad (24)$$

4. Port/starboard, fore/aft and bottom/top symmetries

$$M_a = \begin{bmatrix} m_{a_{11}} & 0 & 0 & 0 & 0 & 0 \\ 0 & m_{a_{22}} & 0 & 0 & 0 & 0 \\ 0 & 0 & m_{a_{33}} & 0 & 0 & 0 \\ 0 & 0 & 0 & m_{a_{44}} & 0 & 0 \\ 0 & 0 & 0 & 0 & m_{a_{55}} & 0 \\ 0 & 0 & 0 & 0 & 0 & m_{a_{66}} \end{bmatrix} \quad (25)$$

The simplifications can go on further for radial symmetries, which are appropriate for cylindrical or spherical bodies.

The magnitude of the function elements of $M_a(\omega)$ and $D(\omega)$ depends on the main dimension of the cross profile, which is perpendicular to the considered direction of the mode. For example, in a spar buoy with radial port/starboard and fore/aft symmetries (see Fig. 2), the added mass and potential damping induced by roll and pitch motions are very important (see Figs. 3–8), while in a semisubmersible with only port/starboard symmetry (see Fig. 9), the added mass and potential damping induced by a yaw motion are the most significant (see Figs. 10–17). Moreover, comparing both cases, the profile of a spar buoy is much more simple than that of a semisubmersible, leading consequently in the last case to the presence of many resonance peaks in the elements in frequency domain.

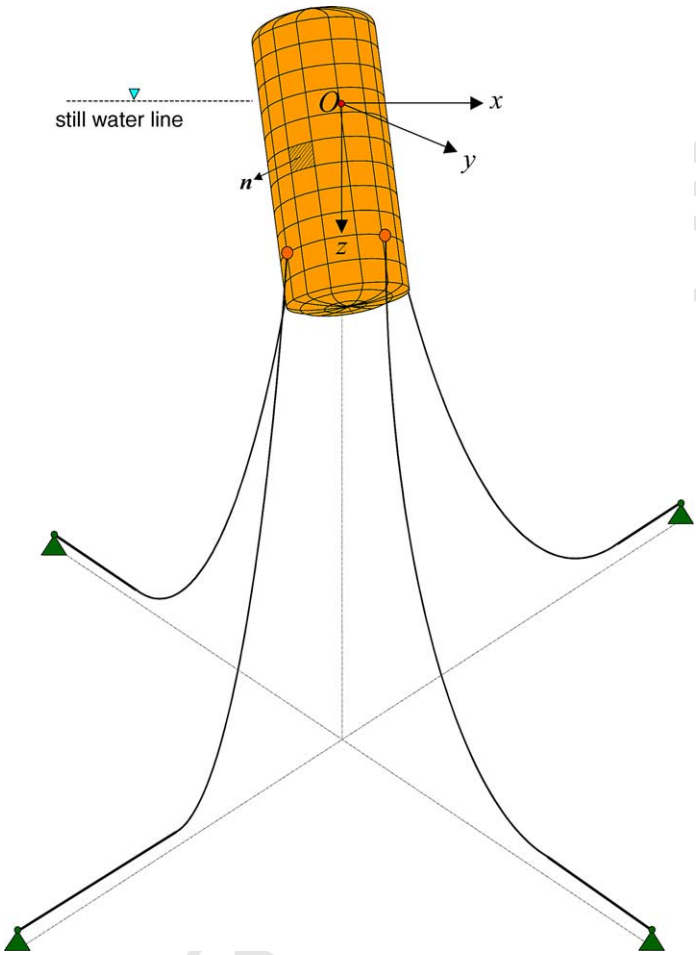

Fig. 2. Moored OE system spar buoy.

4. Reconstruction of $M_a(\omega)$ and $D(\omega)$

It is assumed that the matrices $M_a(\omega)$ and $D(\omega)$ are provided from numerical programs for hydrodynamic analysis and behaviour simulation. However, they are obtained at only a finite (often not large enough) number of frequency samples $\omega_i \in (0, \infty)$. So some reconstruction procedures can be used in order to convert the sequences of numbers $\{M_a(\omega_i)\}$ and $\{D(\omega_i)\}$ into the continuous-frequency matrix functions $M_a(\omega)$ and $D(\omega)$.

Three different reconstructions are discussed in this section.

4.1. Shannon reconstruction

If the sequences $\{M_a(i\omega_0)\}$ and $\{D(i\omega_0)\}$ are obtained at equally spaced points $i\omega_0$ with $i \in \Im$, then the so-called Shannon reconstruction can be applied (Aström and Wittenmark, 1996) to retrieve the added mass and potential damping as

$$M_a(\omega) = \sum_{i=-\infty}^{\infty} M_a(i\omega_0) \frac{\sin((\omega - i\omega_0)/\omega_0/\pi)}{(\omega - i\omega_0)/\omega_0/\pi} \tag{26}$$

$$D(\omega) = \sum_{i=-\infty}^{\infty} D(i\omega_0) \frac{\sin((\omega - i\omega_0)/\omega_0/\pi)}{(\omega - i\omega_0)/\omega_0/\pi}, \tag{27}$$

for $\omega \in [0, \infty]$.

The Shannon reconstruction cannot be applied if the samples are not equally spaced. Besides in (26)–(27), it was used in the symmetry property $M_a(i\omega_0) = M_a(-i\omega_0)$ and the skew-symmetry property $D(i\omega_0) = -D(-i\omega_0)$ in order to avoid errors in the reconstruction of $M_a(\omega)$ and $D(\omega)$ for small frequencies (border effect). The contribution of every weighting function $\sin((\omega - i\omega_0)/\omega_0/\pi)/(\omega - i\omega_0)/\omega_0/\pi$ is maximal at $\omega = i\omega_0$, but it becomes asymptotically smaller for frequencies away from $i\omega_0$. For instance, this contribution is smaller than 5% of $\{M_a(i\omega_0)\}$ (or $\{D(i\omega_0)\}$) for $\omega \leq (i-6)\omega_0$ and $\omega \geq (i+6)\omega_0$. It is to be mentioned that the border effect is unavoidable for large frequencies, because of the trunc-

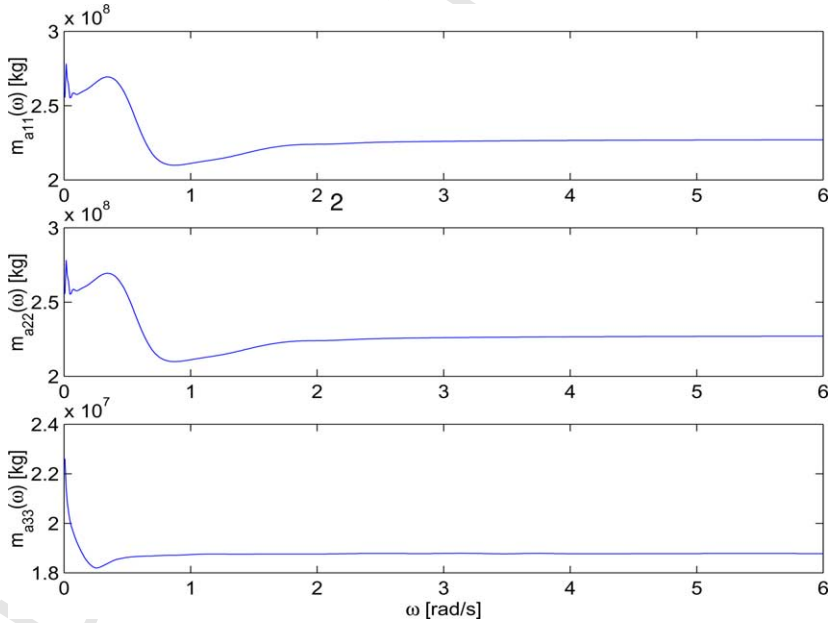

Fig. 3. Elements $m_{a_{11}}(\omega)$, $m_{a_{22}}(\omega)$ and $m_{a_{33}}(\omega)$ of $M_a(\omega)$ of a spar buoy.

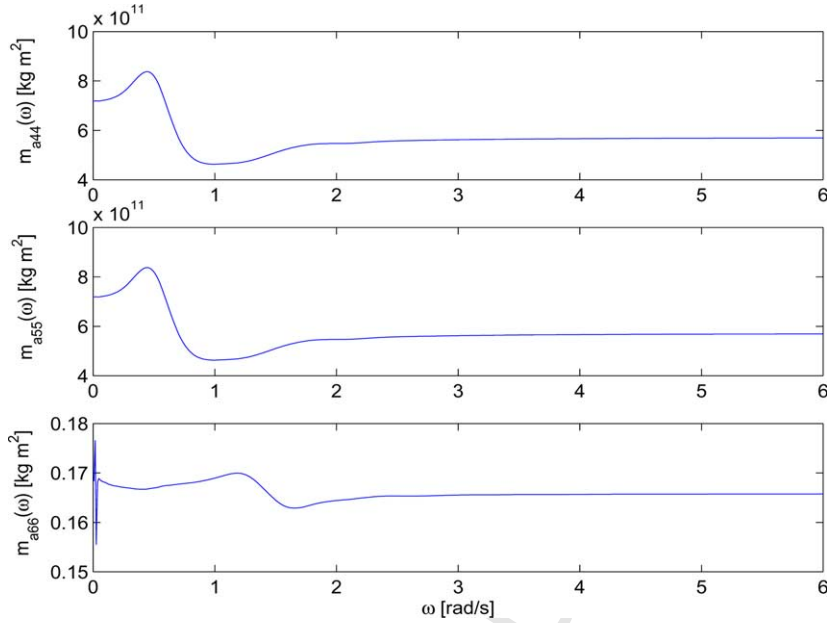

Fig. 4. Elements $m_{a_{44}}(\omega)$, $m_{a_{33}}(\omega)$ and $m_{a_{66}}(\omega)$ of $M_a(\omega)$ of a spar buoy.

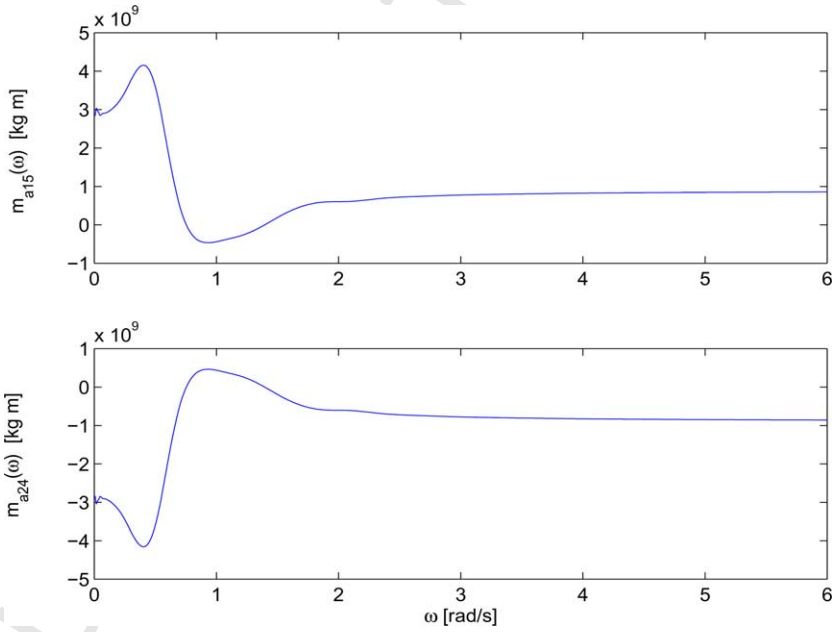

Fig. 5. Elements $m_{a_{15}}(\omega)$ and $m_{a_{24}}(\omega)$ of $M_a(\omega)$ of a spar buoy.

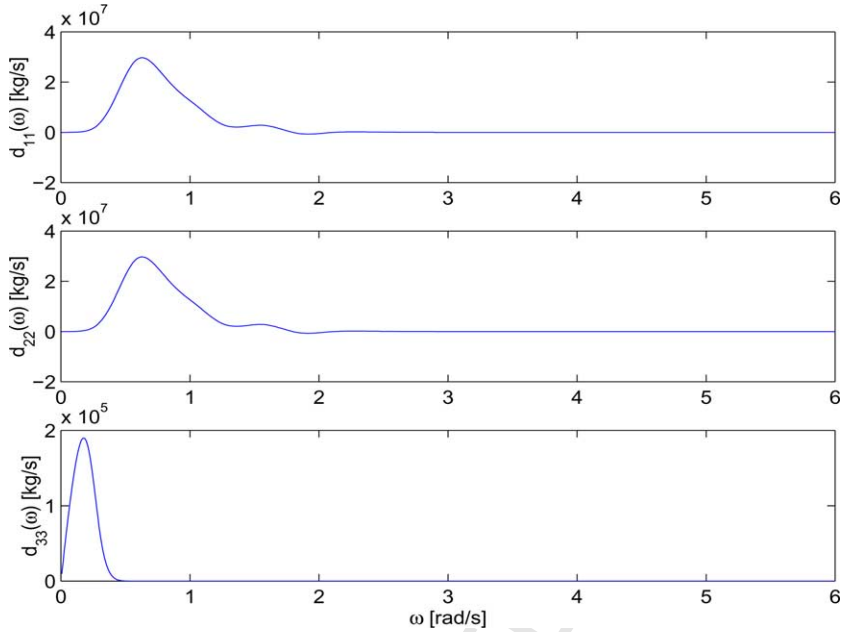

Fig. 6. Elements $d_{11}(\omega)$, $d_{22}(\omega)$ and $d_{33}(\omega)$ of $D(\omega)$ of a spar buoy.

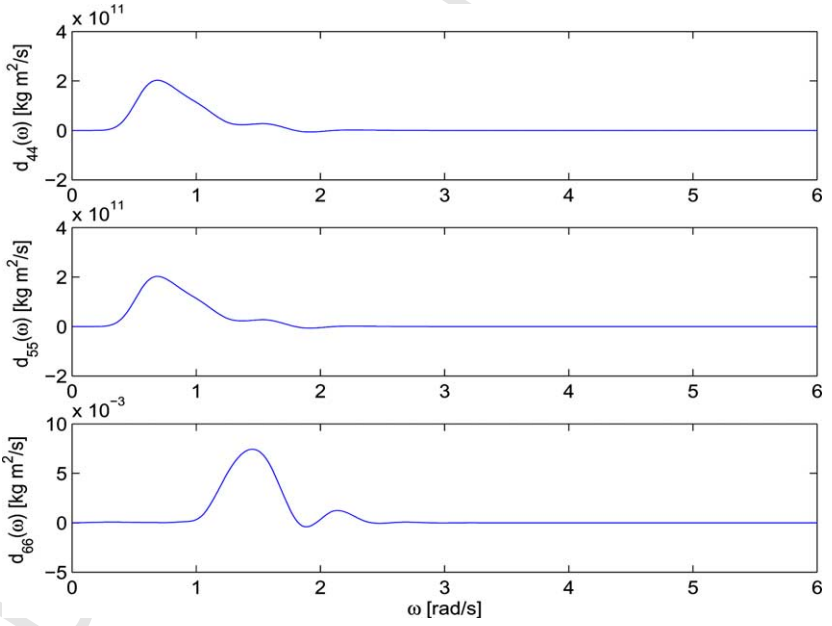

Fig. 7. Elements $d_{44}(\omega)$, $d_{55}(\omega)$ and $d_{66}(\omega)$ of $D(\omega)$ of a spar buoy.

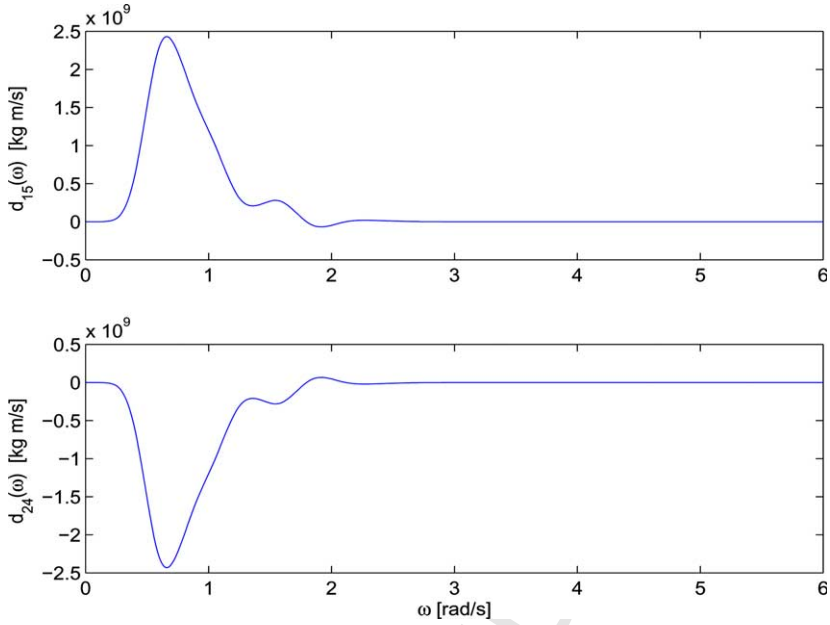

Fig. 8. Elements $d_{15}(\omega)$ and $d_{24}(\omega)$ of $D(\omega)$ of a spar buoy.

ation of the sequences $\{M_a(i\omega_0)\}$ and $\{D(i\omega_0)\}$ for large i's and the contribution of infinite weighting functions to the right of the end frequency.

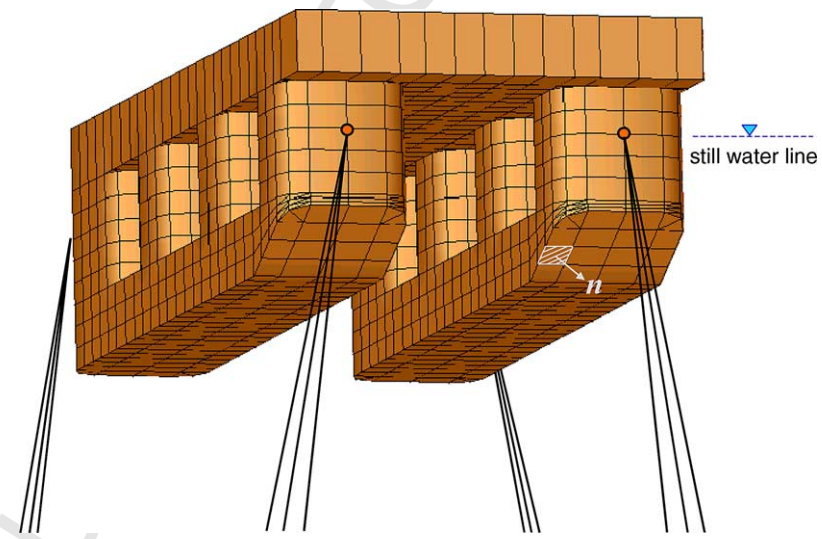

Fig. 9. Moored OE system semisubmersible THIALF.

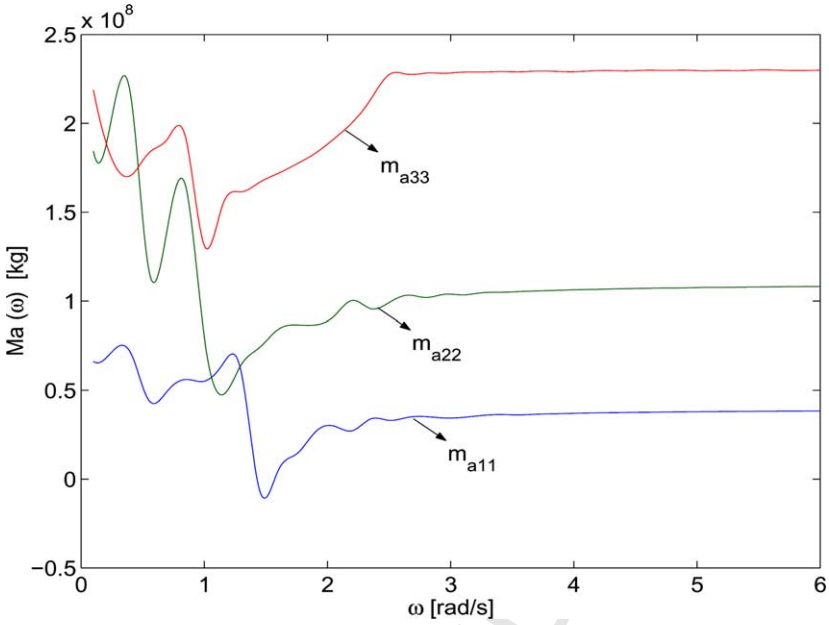

Fig. 10. Elements $m_{a_{11}}(\omega)$, $m_{a_{22}}(\omega)$ and $m_{a_{33}}(\omega)$ of $M_a(\omega)$ of a semisubmersible.

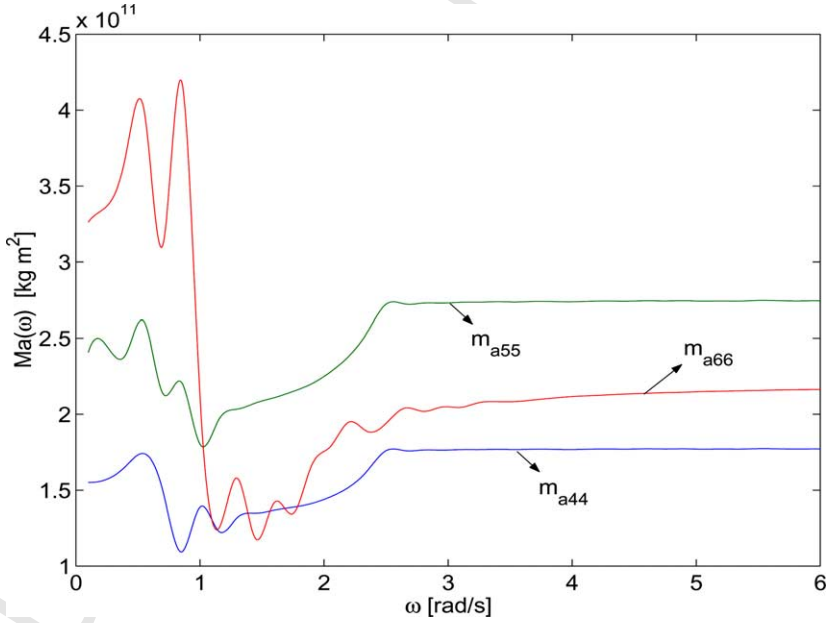

Fig. 11. Elements $m_{a_{44}}(\omega)$, $m_{a_{55}}(\omega)$ and $m_{a_{66}}(\omega)$ of $M_a(\omega)$ of a semisubmersible.

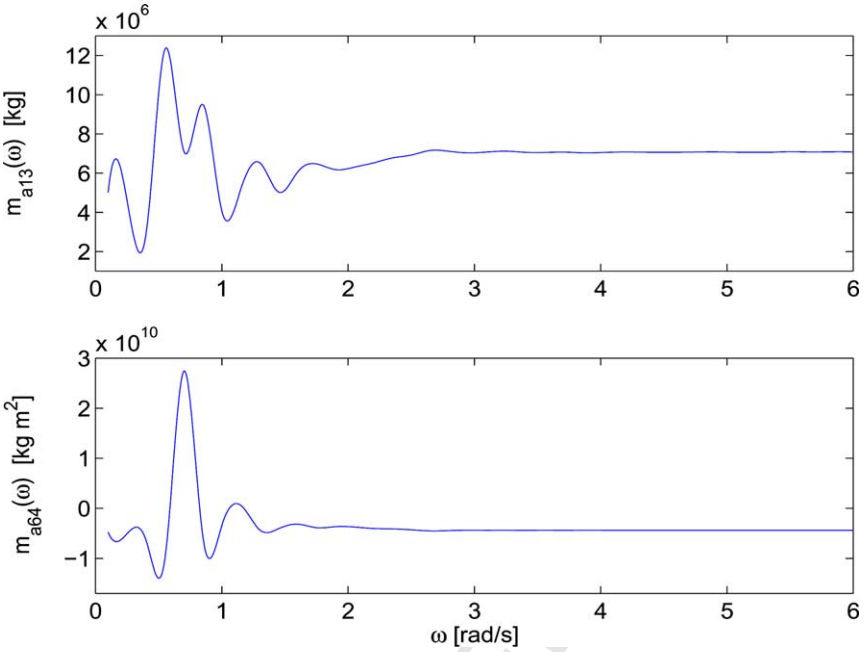

Fig. 12. Elements $m_{a_{13}}(\omega)$ and $m_{a_{64}}(\omega)$ of $M_a(\omega)$ of a semisubmersible.

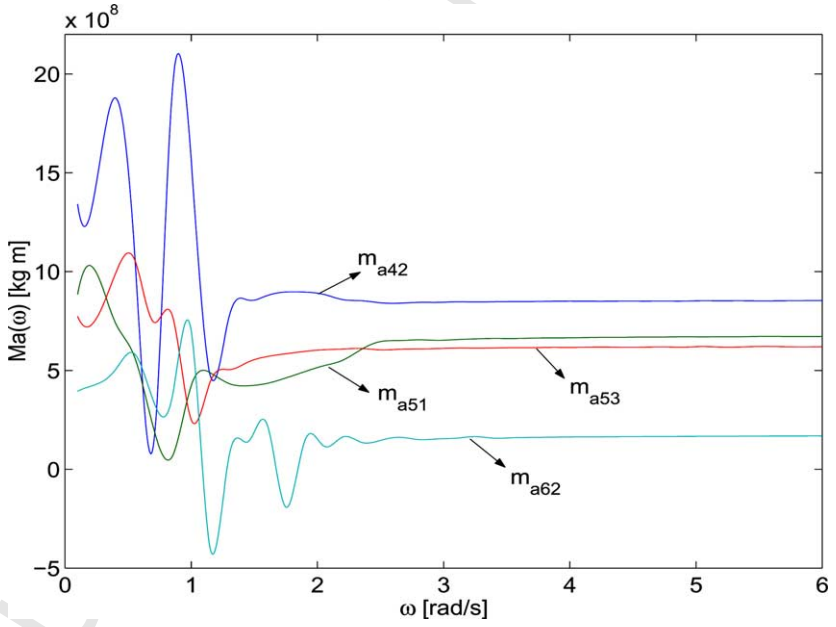

Fig. 13. Elements $m_{a_{42}}(\omega)$, $m_{a_{51}}(\omega)$, $m_{a_{53}}(\omega)$ and $m_{a_{62}}(\omega)$ of $M_a(\omega)$ of a semisubmersible.

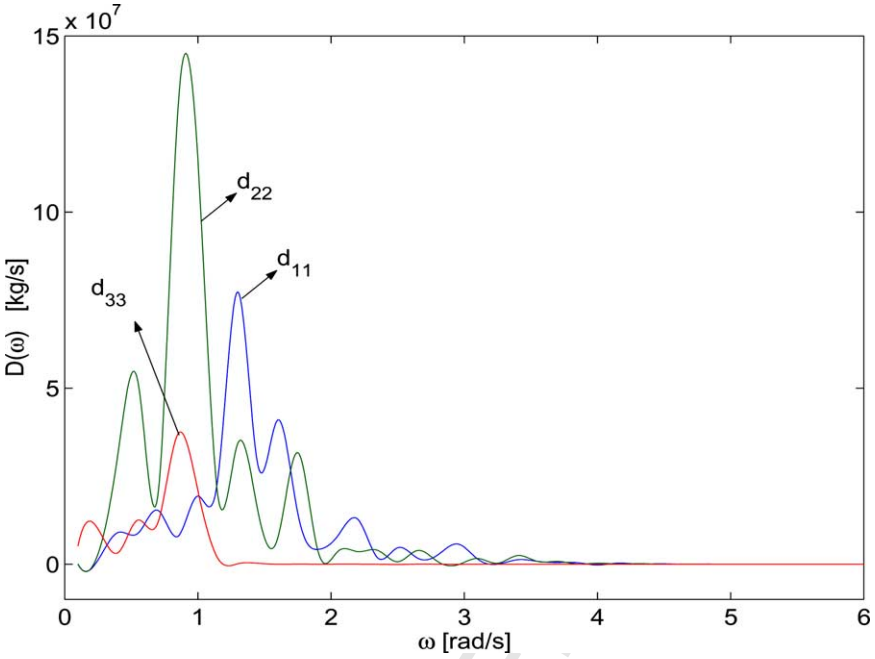

Fig. 14. Elements $d_{11}(\omega)$, $d_{22}(\omega)$ and $d_{33}(\omega)$ of $D(\omega)$ of a semisubmersible.

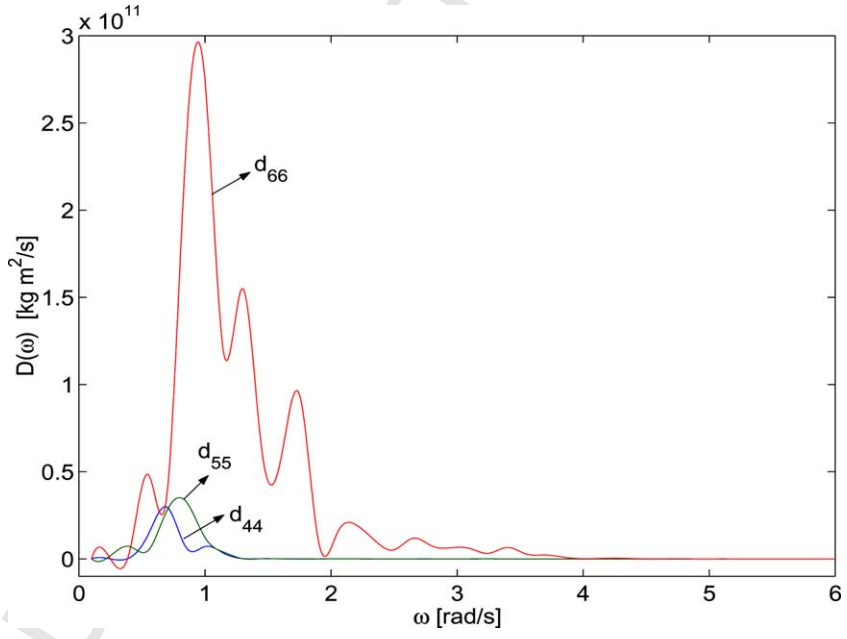

Fig. 15. Elements $d_{44}(\omega)$, $d_{55}(\omega)$ and $d_{66}(\omega)$ of $D(\omega)$ of a semisubmersible.

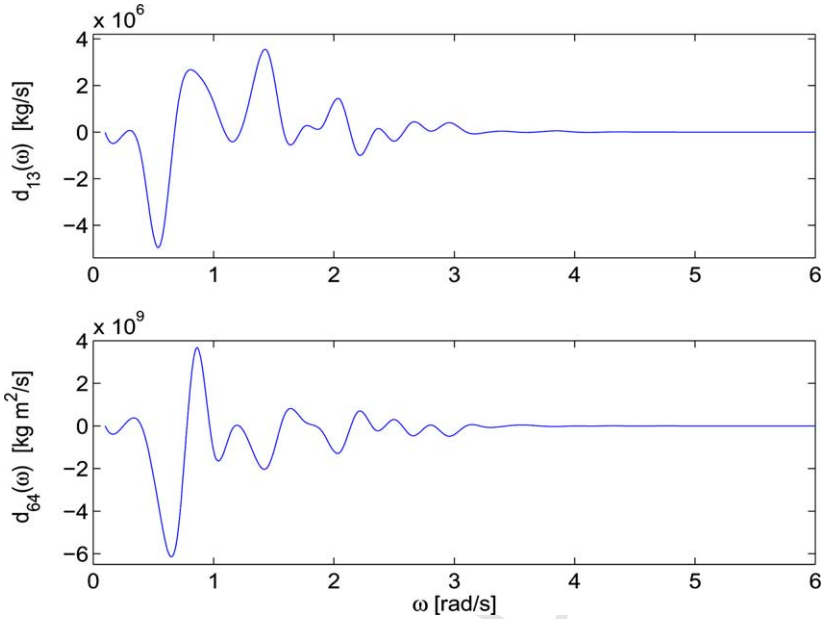

Fig. 16. Elements $d_{13}(\omega)$ and $d_{64}(\omega)$ of $D(\omega)$ of a semisubmersible.

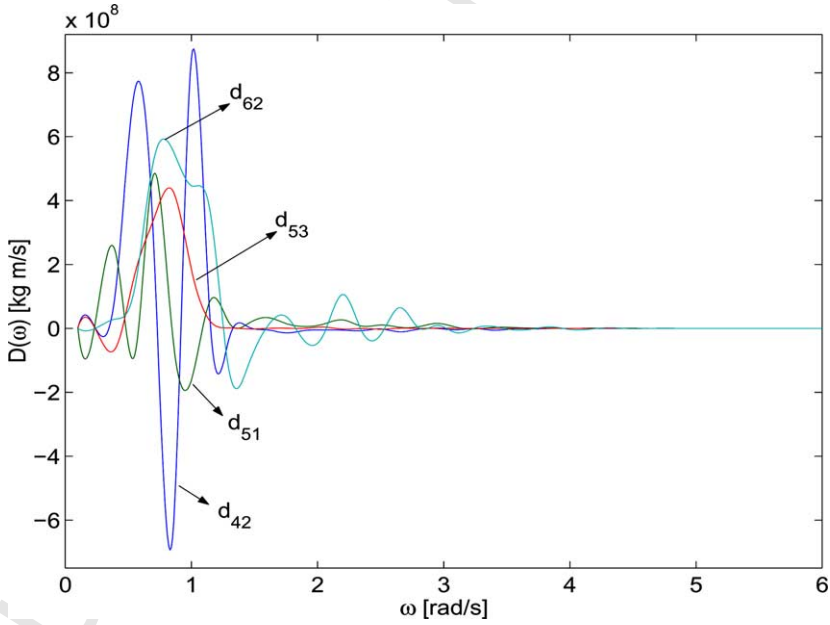

Fig. 17. Elements $d_{42}(\omega)$, $d_{51}(\omega)$, $d_{53}(\omega)$ and $d_{62}(\omega)$ of $D(\omega)$ of a semisubmersible.

4.2. Piecewise-constant reconstruction

For not necessarily regular sampled sequences $M_a(\omega_i)$ and $D(\omega_i)$, one applies in the interval $[\omega_i, \omega_{i+1}]$, a simple step-forward reconstruction for $i = 0, 1, \ldots$ as

$$M_a(\omega) = M_a(\omega_i) \quad \text{for } \omega_i \le \omega \le \omega_{i+1} \tag{28}$$

$$D(\omega) = D(\omega_i) \quad \text{for } \omega_i \le \omega \le \omega_{i+1}, \tag{29}$$

or alternatively, for $i = 1, 2, \ldots$, a step-backward reconstruction

$$M_a(\omega) = M_a(\omega_i) \quad \text{for } \omega_{i-1} \le \omega \le \omega_i \tag{30}$$

$$D(\omega) = D(\omega_i) \quad \text{for } \omega_{i-1} \le \omega \le \omega_i. \tag{31}$$

Assuming $M_a(\omega)$ and $D(\omega)$ have smooth first derivatives, the largest value of the error is given, for instance for the step-forward reconstruction and regular sampling $\omega_i = i\omega_0$, by

$$\varepsilon_{M_a} = \max_{i \in \Im_0^+} |M_a((i+1)\omega_0) - M_a(\omega_0)| \le \omega_0 \max_{\omega \in [0,\infty]} \left| \frac{dM_a(\omega)}{d\omega} \right| \tag{32}$$

$$\varepsilon_D = \max_{i \in \Im_0^+} |D((i+1)\omega_0) - D(\omega_0)| \le \omega_0 \max_{\omega \in [0,\infty]} \left| \frac{dD(\omega)}{d\omega} \right|. \tag{33}$$

The smoother is the evolution of the frequency functions, the smaller is the reconstruction error and smaller is ω_0. This reconstruction has the advantage that it can be used for nonregular sampling. Additionally, the truncation of the sequences $\{M_a(\omega_i)\}$ and $\{D(\omega_i)\}$ for large values of the samples ω_i does not affect the reconstruction aside from the errors (32)–(33).

4.3. Piecewise-cubic reconstruction

This approach consists in a cubic-spline data interpolation. For not necessarily regular sampled sequences $M_a(\omega_i)$ and $D(\omega_i)$, one applies in the interval $[\omega_i, \omega_{i+1}]$ the splines

$$m_{a_{jk}}(\omega) = \alpha_{jk}(\omega - \omega_i)^3 + \beta_{jk}(\omega - \omega_i)^2 + \gamma_{jk}(\omega - \omega_i) + \delta_{jk} \tag{34}$$

$$d_{jk}(\omega) = \zeta_{jk}(\omega - \omega_i)^3 + \eta_{jk}(\omega - \omega_i)^2 + \mu_{jk}(\omega - \omega_i) + \nu_{jk}, \tag{35}$$

The spline coefficient set $\{\alpha_{jk}, \ldots, \nu_{jk}\}$ is attained in a least-squares-error sense from

$$\begin{bmatrix} \alpha_{jk} \\ \beta_{jk} \\ \gamma_{jk} \\ \delta_{jk} \\ \zeta_{jk} \\ \eta_{jk} \\ \mu_{jk} \\ \nu_{jk} \end{bmatrix} = \begin{bmatrix} \Omega(\omega) & 0 \\ 0 & \Omega(\omega) \end{bmatrix} \begin{bmatrix} m_{a_{jk}}(\omega_{i-2}) \\ m_{a_{jk}}(\omega_{i-1}) \\ m_{a_{jk}}(\omega_{i+1}) \\ m_{a_{jk}}(\omega_{i+2}) \\ d_{jk}(\omega_{i-2}) \\ d_{jk}(\omega_{i-1}) \\ d_{jk}(\omega_{i+1}) \\ d_{jk}(\omega_{i+2}) \end{bmatrix}, \tag{36}$$

with

$$\Omega = \begin{bmatrix} (\omega_{i-2}-\omega_i)^3 & (\omega_{i-2}-\omega_i)^2 & (\omega_{i-2}-\omega_i) & 1 \\ (\omega_{i-1}-\omega_i)^3 & (\omega_{i-1}-\omega_i)^2 & (\omega_{i-1}-\omega_i) & 1 \\ (\omega_{i+1}-\omega_i)^3 & (\omega_{i+1}-\omega_i)^2 & (\omega_{i+1}-\omega_i) & 1 \\ (\omega_{i+2}-\omega_i)^3 & (\omega_{i+2}-\omega_i)^2 & (\omega_{i+2}-\omega_i) & 1 \end{bmatrix}^{-1}. \tag{37}$$

The existent border conditions at the beginning and the end, i.e., for $j = 1, 2, \ldots$ and for $j = N_\omega - 1, N_\omega - 2$, are solved especially by taking the four samples on the right side and on the left side, respectively. For the rest of ω_i, Eq. (36) applies straightforwardly with validity in the respective interval $[\omega_i, \omega_{i+1}]$.

The largest error when using cubic interpolation is

$$\varepsilon_{m_{a_{jk}}} = \max_{i\in\Im^+}\max_{\omega\in\Re_0^+}\left|m_{a_{jk}}(\omega) - \alpha_{jk}(\omega-\omega_i)^3 - \beta_{jk}(\omega-\omega_i)^2 - \gamma_{jk}(\omega-\omega_i) - \delta_{jk}\right| \tag{38}$$

$$\varepsilon_{d_{jk}} = \max_{i\in\Im^+}\max_{\omega\in\Re_0^+}\left|d_{jk}(\omega) - \zeta_{jk}(\omega-\omega_i)^3 - \eta_{jk}(\omega-\omega_i)^2 - \mu_{jk}(\omega-\omega_i) - \nu_{jk}\right|. \tag{39}$$

For regular sampling $\omega_i = i\omega_0$, the error can be estimated for at least four times differentiable $M_a(\omega)$ and $D(\omega)$ as

$$\varepsilon_{m_{a_{jk}}} \le \omega_0^4 \max_{\omega\in[0,\infty]}\left|\frac{d^4\left(m_{a_{jk}}(\omega)\right)}{d\omega^4}\right| \tag{40}$$

$$\varepsilon_{d_{jk}} \le \omega_0^4 \max_{\omega\in[0,\infty]}\left|\frac{d^4\left(d_{jk}(\omega)\right)}{d\omega^4}\right|. \tag{41}$$

For small ω_0, the error is bounded considerably especially for smooth functions $M_a(\omega)$ and $D(\omega)$. Similarly as in the former procedure, the truncation of the sequences $\{M_a(\omega_i)\}$ and $\{D(\omega_i)\}$ for large values of the samples ω_i does not affect the reconstruction apart from the errors (38)–(39) and the mentioned local border effect at the end frequency. The other main advantage of this reconstruction is the analyticity of the approximated function, whose integral or derivative can be computed exactly. The main disadvantage is that the procedure is complicated to implement, and cumbersome and time-consuming to apply.

5. Existing approach: convolution model

Two approaches will be described to characterise the radiation-induced hydrodynamics under the Potential Flow Theory, namely the nonparametric convolution approach and the parametric state-space approach.

They are explored from the points of view of representation, identification and stability.

5.1. Representation

Taking (13) or (14) into account, the functional matrix $K(\tau)$, $\tau \in [0, \infty]$ represents a nonparametric characteristic of the potential-radiation hydrodynamics. It depends only on the geometry of the submersed part of the structure. It is defined as the impulse response of the so-called regular hydrodynamic radiation force

$$\mathbf{s}_0 = \mathbf{F}_R(t) + M_\infty \ddot{\mathbf{q}}(t). \tag{42}$$

over the wet hull for the fluid-structure at rest, due to an impulsive velocity

$$\dot{\mathbf{q}}(t) = -\delta(t)\dot{\mathbf{q}}(0) = [-\delta(t), \ldots, -\delta(t)]^T, \tag{43}$$

where $\delta(t)$ is the Dirac impulsive function, or equivalently, to a sudden change of position

$$\mathbf{q}(t) = -h(t)\mathbf{q}(0) = [-h(t), \ldots, -h(t)]^T, \tag{44}$$

where $h(t)$ is the Heaviside step function.

Using the Kramers–Kronig relationships (Bracewell, 1978), it is valid

$$D(\omega) = -\frac{2}{\pi}\int_0^\infty \left(\int_0^\infty (M_a(\omega) - M_\infty)\omega \sin(\omega t)\, d\omega\right)\cos(\omega t)\, dt \tag{45}$$

$$M_a(\omega) - M_\infty = -\frac{2}{\pi\omega}\int_0^\infty \left(\int_0^\infty D(\omega)\cos(\omega t)\, d\omega\right)\sin(\omega t)\, dt, \tag{46}$$

from which is follows the impulse function matrix

$$K(\tau) = \frac{2}{\pi}\int_0^\infty D(\omega)\cos(\omega\tau)\, d\omega \tag{47}$$

$$= \frac{2}{\pi}\int_0^\infty (M_a(\omega) - M_\infty)\omega\sin(\omega\tau)\, d\omega. \tag{48}$$

Besides, if $K(\tau)$ is absolutely integrable, the following properties can be drawn out using the Riemann–Lebesgue Lema (Ogilvie, 1964)

$$\lim_{\omega\to\infty}\int_0^\infty K(\tau)\sin(\omega\tau)\, d\tau \tag{49}$$

$$= \lim_{\omega\to\infty}\int_0^\infty K(\tau)\cos(\omega\tau)\, d\tau = 0 \tag{50}$$

$$\lim_{\omega\to 0}\frac{1}{\omega}\int_0^\infty K(\tau)\sin(\omega\tau)\, d\tau \tag{51}$$

$$= \lim_{\omega\to 0}\int_0^\infty K(\tau)\cos(\omega\tau)\, d\tau \tag{52}$$

$$= \int_0^\infty K(\tau)\, d\tau < \infty. \tag{53}$$

Eqs. (49)–(50) show the continuity and boundness of $K(\tau)$, while (53) gives evidence of the stability of the hydrodynamics of the fluid-structure, i.e., it establishes that the radiation-induced force over the hull will asymptotically vanish in time after a sudden motion of the structure from rest in an environment also at rest.

In Fig. 18 the elements corresponding to the principal diagonal of $K(t)$ matrix for the OE system spar buoy are depicted. Analogously in Figs. 19–20, the elements for an OE system semisubmersible platform are seen.

5.2. Identification

The identification consists in calculating the impulse function matrix $K(\tau)$ by means of (47) or (48). As the integral in (47) is less cumbersome, we adopt this way. For the element jk of $K(\tau)$ one gets

$$k_{jk}(\tau) = \frac{2}{\pi}\int_0^\infty d_{jk}(\omega)\cos(\omega\tau)\,\mathrm{d}\omega. \tag{54}$$

The piecewise-constant and the piecewise-cubic reconstructions are appropriate for implementing the integrated function analytically. For instance, the piecewise-constant step-forward reconstruction for N_ω samples gives

$$k_{jk}(\tau) = \frac{2}{\pi}\sum_{i=1}^{N_\omega}\frac{d_{jk}(\omega_i)}{\tau}(\sin(\omega_{i+1}\tau) - \sin(\omega_i\tau)). \tag{55}$$

On the other side, the cubic interpolation for N_ω samples produces

$$\begin{aligned} k_{jk}(\tau) = \frac{2}{\pi}\sum_{i=1}^{N_\omega}\frac{1}{\tau^4}\big(&\big(6e_{kj} - g_{kj}\tau^2\big)\cos(\omega_i\tau) + \big(3e_{kj}\big(-2+\tau^2(\omega_i-\omega_{i+1})^2\big)\\ &+\tau^2\big(g_{kj}+2f_{kj}(\omega_{i+1}-\omega_i)\big)\big)\cos(\omega_{i+1}\tau) + \tau\big(\big(2f_{kj}-h_{kj}\tau^2\big)\sin(\omega_i\tau)\\ &+\big(h_{kj}\tau^2 + f_{kj}\big(-2+\tau^2(\omega_i-\omega_{i+1})^2\big) - \big(g_{kj}\tau^2 + e_{kj}\big(-6+\tau^2(\omega_i-\omega_{i+1})^2\big)\big)\\ &\times(\omega_i-\omega_{i+1})\big)\sin(\omega_{i+1}\tau)\big)\big). \end{aligned} \tag{56}$$

As the determination of $K(\tau)$ is usually carried out with the purpose of further digital processing and simulation, the identification will require the evaluation of (55) or (56) for discrete values $\tau_i \in [0, T_K]$, where T_K is some common settling time for all elements, obtained from

$$\big|k_{jk}(\tau_i) - k_{jk}(\tau_{i-1})\big| \le 0.01 \max_{\tau_i\in[0,T_K]j,k=1,\ldots,6} k_{jk}(\tau_i) \tag{57}$$

where 1% of the maximal value of $k_{jk}(\tau_i)$ in (57) fits well in the applications. Finally, the result of the nonparametric estimation is a matrix sequence $\{K(\tau_i)\}$ with $\tau_i \in [0, T_K]$.

5.3. Stability

The dynamic stability of the fluid-structure hydrodynamics is inherently ensured by physical laws. This stability is reflected by the fact that $K(\tau)$ tends asymptoti-

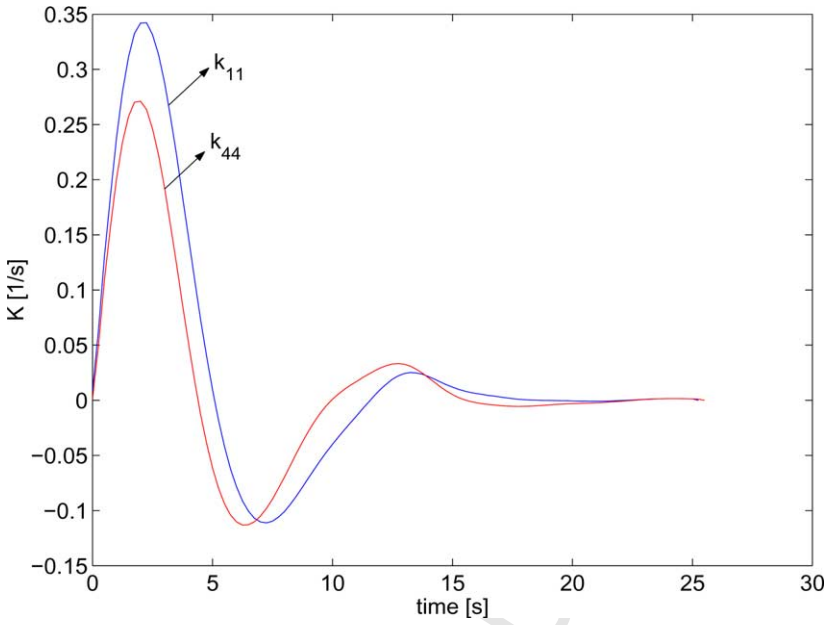

Fig. 18. Elements $k_{11}(t) = k_{22}(t)$, $k_{33}(t)$ and $k_{44}(t) = k_{55}(t)$ of the $K(t)$ for a spar buoy.

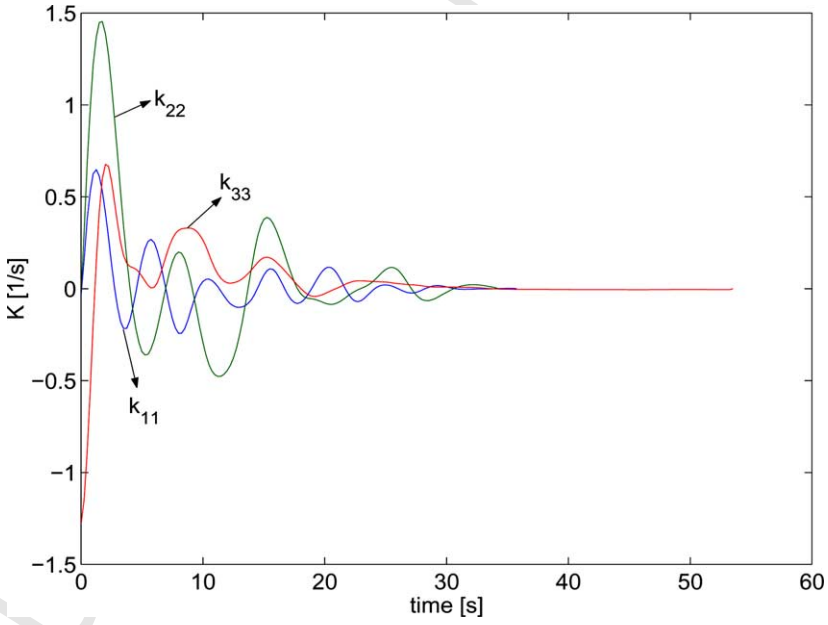

Fig. 19. Elements $k_{11}(t)$, $k_{22}(t)$ and $k_{33}(t)$ of the $K(t)$ for a semisubmersible.

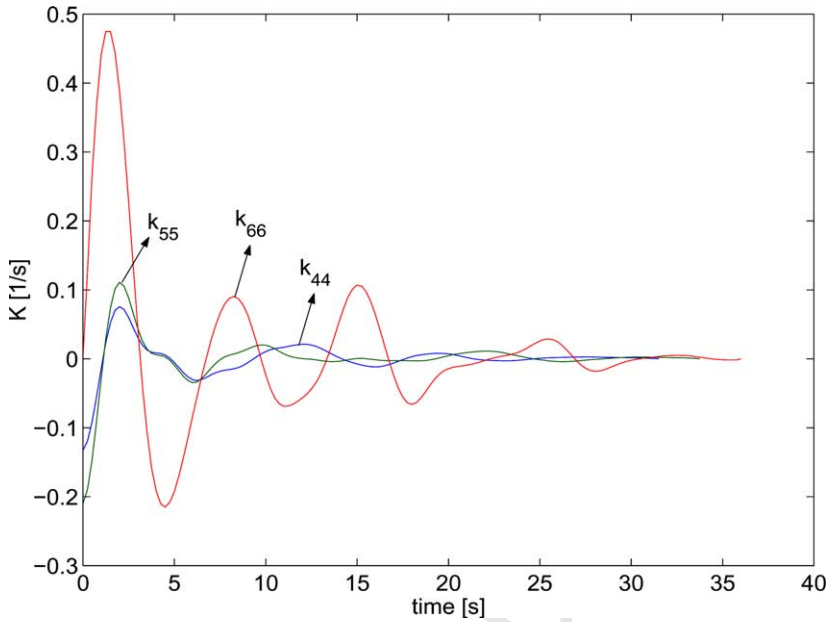

Fig. 20. Elements $k_{44}(t)$, $k_{55}(t)$ and $k_{66}(t)$ of the $K(t)$ for a semisubmersible.

cally to zero. This can be proved using the property of $D(\omega)$ of being continuous (cf. (49)–(50)), so one gets

$$\lim_{\tau\to\infty} K(\tau) = \lim_{\tau\to\infty} \frac{2}{\pi}\int_0^\infty D(\omega)\cos(\omega\tau)\,\mathrm{d}\omega \tag{58}$$

$$= \lim_{\tau\to\infty} \frac{2}{\pi}\int_0^\infty D(\omega)\alpha(\omega\tau)\,\mathrm{d}\omega \tag{59}$$

$$= 0, \tag{60}$$

where

$$\alpha(\omega\tau) = \begin{cases} 1, & \text{if} \quad \cos(\omega\tau) \geq 0 \\ -1, & \text{otherwise} \end{cases}. \tag{61}$$

Hence the numerical stability of the sequence $\{K(\tau_i)\}$ for every $\tau_i \in [0,\infty]$ is ensured for every reconstruction type and one fulfills

$$\lim_{\tau_i\to\infty} K(\tau_i) = 0. \tag{62}$$

6. Existing approach: state-space model of Jiang

6.1. Representation

Eq. (17) can be stated as (Jiang, 1991; Schelin et al., 1993)

$$\mathbf{F}_{\mathrm{R}}(\dot{\mathbf{q}},\ddot{\mathbf{q}}) = -M_{\infty}\ddot{\mathbf{q}} + \mathbf{s}_0, \tag{63}$$

where $\mathbf{s}_0$ stands for the regular part of the radiation force and is described in frequency domain by

$$\mathbf{s}_0(\mathrm{j}\omega) = (-D(\omega) - \mathrm{j}\omega(M_{\mathrm{a}}(\omega) - M_{\infty}))\dot{\mathbf{q}}(j\omega). \tag{64}$$

and in time domain by

$$\mathbf{s}_0(t) = -\int_{-\infty}^{t} K(t-\tau)\dot{\mathbf{q}}(\tau)\,\mathrm{d}\tau = -\int_{0}^{t} K(\dot{\tau})\dot{\mathbf{q}}(t-\tau)\,\mathrm{d}\tau \tag{65}$$

The $\mathbf{s}_0$ accomplishes for the memory dependence of the force with the fluid motion.

The right side of (64) can be approximated by a matrix polynomial as

$$\mathbf{s}_0(\mathrm{j}\omega) \cong -\left[(\mathrm{j}\omega)^{n+1}I + \sum_{l=0}^{n}(\mathrm{j}\omega)^{l}A_l\right]^{-1}\left[\sum_{l=0}^{n}(\mathrm{j}\omega)^{l}B_l\right]\dot{\mathbf{q}}, \tag{66}$$

where n is the order of the approximation.

Assuming equality in (66), passing the matrices $(\mathrm{j}\omega)^{l}A_l$ and $(\mathrm{j}\omega)^{n+1}I$ in (66) to the left side and dividing the all terms by $(\mathrm{j}\omega)^{n}$, the following state-space representation can be deduced

$$\begin{cases} \dot{\mathbf{s}}_0 = \mathbf{s}_1 - A_n\mathbf{s}_0 - B_n\dot{\mathbf{q}} \\ \vdots \\ \dot{\mathbf{s}}_{n-1} = \mathbf{s}_n - A_1\mathbf{s}_0 - B_1\dot{\mathbf{q}} \\ \dot{\mathbf{s}}_0 = -A_0\mathbf{s}_0 - B_0\dot{\mathbf{q}} \end{cases}, \tag{67}$$

where $\mathbf{s}_0,\ldots,\mathbf{s}_n$ are the so-called hydrodynamic states, and A_l and B_l are constant matrices of the representation.

The stability of (67) will be important for the next development of an algorithm for optimal identification of A_l and B_l.

6.2. Stability

As (66) is an approximation of (64), the stability of (67) must be tested because the model may be unstable. To this goal, (67) can be stated as

$$\dot{\mathbf{y}}_{\mathrm{s}}(t) = A_{\mathrm{s}}\mathbf{y}_{\mathrm{s}}(t) + B_{\mathrm{s}}\dot{\mathbf{q}}(t), \tag{68}$$

with

$$\mathbf{y}_{\mathrm{s}}(t) = \begin{bmatrix} \mathbf{s}_0^{\mathrm{T}} & \mathbf{s}_1^{\mathrm{T}} & \dots & \mathbf{s}_n^{\mathrm{T}} \end{bmatrix}^{\mathrm{T}}, \tag{69}$$

$$B_{\mathrm{s}} = \begin{bmatrix} -B_n & -B_{n-1} & \dots & -B_1 & -B_0 \end{bmatrix}^{\mathrm{T}}, \tag{70}$$

$$A_{\mathrm{s}} = \begin{pmatrix} -A_n & I & 0 & \dots & 0 \\ -A_{n-1} & 0 & I & \dots & 0 \\ \vdots & & \dots & \ddots & \vdots \\ -A_1 & 0 & \dots & 0 & I \\ -A_0 & 0 & \dots & 0 & 0 \end{pmatrix}. \tag{71}$$

So, the hydrodynamic model is asymptotically stable if and only if A_{s} has all its eigen-values with negative real part.

6.3. Identification

The identification problem consists in determining the constant symmetric matrices A_l and B_l upon data $M_{\mathrm{a}}(\omega)$ and $D(\omega)$.

Notice first that the space-state model is characterized by constant symmetric $[6 \times 6]$-matrices A_l and B_l, for $l = 0, \dots, n$, leading to $72(n+1)$ undetermined coefficient. Due to the large number of unknown parameters, a bad conditioned estimation problem in a least-squares sense in frequency domain is expected. In order to make the identification in this sense possible, some counteractive measures must be undertaken.

In this paper, a discrete least-squares estimation method of the sets $\{A_l\}$ and $\{B_l\}$ is presented. The information contained in the frequency-discrete raw data $M_{\mathrm{a}}(\omega_i)$, M_∞ and $D(\omega_i)$ is generally not sufficient to achieve this goal. So a reconstruction procedure upon the raw data is consequently necessary. After frequency-continuous functions $M_{\mathrm{a}}(\omega)$, M_∞ and $D(\omega)$ are found, transmitted asymmetries from raw data are eradicated using instead

$$\frac{M_{\mathrm{a}}(\omega) + M_{\mathrm{a}}^{\mathrm{T}}(\omega)}{2}, \frac{M_\infty + M_\infty^{\mathrm{T}}}{2}, \frac{D(\omega) + D^{\mathrm{T}}(\omega)}{2}, \tag{72}$$

respectively. Besides, one employs the particular feature of symmetry for the OE system structure and nulls the respective elements $m_{jk}(\omega)$ and $d_{jk}(\omega)$, which round about zero due to numerical imprecisions.

Another measure of achieving a good conditioned estimation consists in introducing a weighting matrix (Jiang, 1991; Schelin et al., 1993)

$$G(L) = \mathrm{diag}(L, L, L, 1, 1, 1), \tag{73}$$

with L is a positive real-valued parameter. According to Jiang (1991), L means the main longitude of the structure.

Assuming the equality in (66) and then multiplying both sides by $G(L)$, one accomplishes

$$\frac{1}{(\mathrm{j}\omega)^{n+1}}\begin{bmatrix} L^2C_{11} & LC_{12} \\ LC_{11} & C_{22} \end{bmatrix} = \tag{74}$$

$$\frac{1}{(\mathrm{j}\omega)^{n+1}}\begin{bmatrix} L^2B_{0_{11}} & LB_{0_{12}} \\ LB_{0_{21}} & B_{0_{22}} \end{bmatrix} + \cdots + \frac{1}{\mathrm{j}\omega}\begin{bmatrix} L^2B_{n_{11}} & LB_{n_{12}} \\ LB_{n_{21}} & B_{n_{22}} \end{bmatrix} - \frac{1}{(\mathrm{j}\omega)^{n+1}} \times \begin{bmatrix} LA_{0_{11}} & LA_{0_{12}} \\ A_{0_{21}} & A_{0_{22}} \end{bmatrix}\begin{bmatrix} LC_{11} & C_{12} \\ LC_{11} & C_{22} \end{bmatrix} - \cdots - \frac{1}{\mathrm{j}\omega}\begin{bmatrix} L^2A_{n_{11}} & LA_{n_{12}} \\ LA_{n_{21}} & A_{n_{22}} \end{bmatrix} \times \begin{bmatrix} LC_{11} & C_{12} \\ LC_{11} & C_{22} \end{bmatrix}, \tag{75}$$

with $A_{l_{11}}, \ldots, A_{l_{22}}$, $B_{l_{11}}, \ldots, B_{l_{22}}$ 3×3-block matrices, which compose A_l and B_l, respectively, and $C_{11}, \ldots, C_{22}$ 3×3-block matrices conforming to $[D(\omega) + \mathrm{j}\omega(M_{\mathrm{a}}(\omega) - M_{\infty})]$.

Let us consider the row j on the right side of (75). The matrix elements involved there and referred to as $a_{l_{jk}}$ and $b_{l_{jk}}$ can be arranged for estimation purposes into the parameter vector of dimension $12(n+1)$

$$\theta_j = \left[b_{0_{j1}}, \ldots, b_{0_{j6}}, \ldots, b_{n_{j1}}, \ldots b_{n_{j6}}, a_{0_{j1}}, \ldots, a_{0_{j6}}, \ldots, a_{n_{j1}}, \ldots, a_{n_{j6}}\right]^{\mathrm{T}}. \tag{76}$$

Using (74)–(75), one constructs a regression equation for the estimation of θ_j as

$$Q_j(L)\mathbf{Y}_j(\omega) = Q_j(L)\Psi_j(\omega)\theta_j. \tag{77}$$

with $\Psi_j(\omega)$ being the so-called regression matrix, $Q_j(L)$ a weighting matrix and $\mathbf{Y}_j(\omega)$ the so-called measured vector.

The regression matrix is composed of 12 different regressors (six real and six imaginary), which are evaluated at N_ω discrete frequencies. It has the dimension $[12N_\omega \times 12(n+1)]$ and looks

$$\Psi_j(\omega) = \left[\phi_{R_{j1}}(\omega_1), \ldots, \phi_{R_{j6}}(\omega_1), \ldots, \phi_{I_{j1}}(\omega_1), \ldots, \phi_{I_{j6}}(\omega_1), \ldots, \phi_{R_{j1}}(\omega_{N_\omega}), \ldots, \times\phi_{R_{j6}}(\omega_{N_\omega}), \ldots, \phi_{I_{j1}}(\omega_{N_\omega}), \ldots, \phi_{I_{j6}}(\omega_{N_\omega})\right]^{\mathrm{T}}, \tag{78}$$

with the real and imaginary regressors

$$\phi_{R_{j1}}(\omega_i) = \left[\frac{-1}{\omega_i^{n+1}}, \ldots, 0, \frac{1}{\omega_i}, \ldots, 0, \frac{d_{j1}(\omega_i)}{\omega_i^{n+1}}, \ldots, \frac{d_{j6}(\omega_i)}{\omega_i^{n+1}}, \ldots, -\frac{d_{j1}(\omega_i)}{\omega_i}, \ldots, -\frac{d_{j6}(\omega_i)}{\omega_i}\right]^{\mathrm{T}}, \tag{79}$$

and

$$\phi_{I_{j1}}(\omega_i) = \left[0, \ldots, \frac{1}{\omega_i^n}, \ldots, 0, \frac{1}{\omega_i^2}, \ldots, 0, \frac{-m_{\mathrm{a}_{j1}}(\omega_i) + m_{\infty_{j1}}}{\omega_i^n}, \ldots, \frac{-m_{\mathrm{a}_{j6}}(\omega_i) + m_{\infty_{j6}}}{\omega_i^n}, \ldots, \times\left(m_{a_{j1}}(\omega_i) - m_{\infty_{j1}}\right), \ldots, \left(m_{\mathrm{a}_{j6}}(\omega_i) - m_{\infty_{j6}}\right)\right]^{\mathrm{T}}, \tag{80}$$

respectively, where $m_{a_{jk}}$, $m_{\infty_{jk}}$ and d_{jk} are elements of M_a, M_∞ and D, respectively. In the development of (79)–(80) an n even was supposed (for n odd the development is analogous).

The weighting matrix $Q_j(L)$ is a square block-diagonal matrix

$$Q_j(L) = \begin{cases} \text{diag}[P_0, \ldots, P_0], & \text{for } j = 1, 2, 3 \\ \text{diag}[P_1, \ldots, P_1], & \text{for } j = 4, 5, 6 \end{cases}, \tag{81}$$

with

$$P_0 = \text{diag}(L^2, L^2, L^2, L, L, L, L^2, L^2, L^2, L, L, L) \tag{82}$$

$$P_1 = \text{diag}(L, L, L, 1, 1, 1, L, L, L, 1, 1, 1). \tag{83}$$

The measure vector is

$$\mathbf{Y}_j(\omega) = \left[\omega_1\left(m_{a_{j1}}(\omega_1) - m_{\infty_{j1}}\right), \ldots, d_{j6}(\omega_1), \ldots, \omega_{N_\omega}\left(m_{a_{j1}}(\omega_{N_\omega}) - m_{\infty_{j1}}\right), \ldots, \times d_{j6}(\omega_{N_\omega})\right]^{\mathrm{T}}. \tag{84}$$

The least-squares solution for the estimation of all θ_j's results

$$\begin{bmatrix} \theta_1 \\ \vdots \\ \theta_6 \end{bmatrix} = \begin{bmatrix} \left[\Psi_1^{\mathrm{T}} Q_1(L) \Psi_1\right]^{-1} \Psi_1^{\mathrm{T}} Q_1(L) \mathbf{Y}_1 \\ \vdots \\ \left[\Psi_6^{\mathrm{T}} Q_6(L) \Psi_1\right]^{-1} \Psi_6^{\mathrm{T}} Q_6(L) \mathbf{Y}_6 \end{bmatrix}. \tag{85}$$

Choosing L as the main longitude of the OE system often does not ensure the best model in least-squares sense (67). Consequently in this paper, we develop a procedure for optimal estimation with respect to a variable parameter. The algorithm performs the optimisation row by row, and thus it uses an optimal variable L_j for every now j of (85).

To this end, one faces a double minimisation for L_j and for the θ_j's by means of

$$\min_{L_j > 0} \min_{\theta_j} \left[Q_j \mathbf{Y}_j - Q_j \Psi_j \theta_j\right]^2 \tag{86}$$

$$= \min_{L_j > 0} \left[Q_j \mathbf{Y}_j - Q_j \Psi_j \left[\Psi_j^{\mathrm{T}} Q_j \Psi_j\right]^{-1} \Psi_j^{\mathrm{T}} Q_j \mathbf{Y}_j\right]^2, \tag{87}$$

which, after some extensive manipulations, leads to the analytical extreme condition

$$L_j^3 \sum_k \alpha_{jk}(\omega) - L_j \sum_k \beta_{jk}(\omega) = 0 \quad \text{for } j = 1, 2, 3, \tag{88}$$

$$L_j \sum_k \beta_{jk}(\omega) = 0 \quad \text{for } j = 4, 5, 6, \tag{89}$$

with the extreme values $L_{0_j} = +\sqrt{\sum_k \beta_{jk} / \sum_k \alpha_{jk}}$ or $L_{0_j} = 0$, respectively, and α_{jk}, β_{jk} frequency-dependent terms for every row j.

However, as all the L_{0_j}'s may not ensure stability of (67), it is recommended performing (87) numerically.

6.4. Suboptimal identification

Therefore, to accomplish stability, a suboptimal solution is generally chosen. So, instead of (87), the following minimisation with constrain is developed (Jordán and Beltán-Aguedo, 2003)

$$\min_{\mathrm{Re}\{\lambda_i(A_s)\}<0} \sum_j \min_{L_j>0} \left[Q_j(L_j)\mathbf{Y}_j - Q_j(L_j)\Psi_j \left[\Psi_j^{\mathrm{T}} Q_j(L_j)\Psi_j \right]^{-1} \Psi_j^{\mathrm{T}} Q_j(L_j)\mathbf{Y}_j \right]^2. \quad (90)$$

which is equivalent to a row-by-row minimisation with constraint on model stability, i.e., it is carried out for every row j separately before testing for stability.

Expression (90) is systematically performed for discretely increasing positive L_j's in some interval $[L_{\min}, L_{\max}]$. The constraint $\mathrm{Re}\{\lambda_i(A_s)\} < 0$ refers to the real part of the eigenvalues of A_s in (71). If this constraint cannot be satisfied during the optimal estimation, it is recommended decreasing the order of the approximation n. However, doing that in order to reach stability, the accuracy of the state-space model is sacrificed.

Another feature of the row-by-row estimation (90) is that it does not assure the symmetry of the estimated matrices A_l and B_l. Hence a simple forced symmetrisation can be conveniently achieved by doing $A_l + A_l^{\mathrm{T}}/2$ and $B_l + B_l^{\mathrm{T}}/2$.

6.5. Mode-dependent optimisation

It is remarkable that the row-by-row optimisation distributes the least square error of each row uniformly onto all elements of itself. In the case where the row elements have different order of magnitudes (as this is often the case in OE systems), the most affected estimations will be the smallest elements in the row.

Often, some motions are more important than others, for instance, the plane motion (x, z, θ) of a semisubmersible, or the roll and pitch motions in a buoy. Moreover, this motion may not correspond to the modes with the highest hydrodynamic gain. In such a case, it is desirable to perform the optimisation mode by a mode that includes only the most significant ones of the particular behaviour. Towards this goal, minimisation with constraint (90) is expressed as

$$\min_{\mathrm{Re}\{\lambda_i(A_s)\}<0} \sum_j P_j \min_{L_j>0} \left[Q_j(L_j)\mathbf{Y}_j - Q(L_j)\Psi_j \left[\Psi_j Q(L_j)\Psi_j \right]_j^{-1} \Psi_j^{\mathrm{T}} Q(L_j)\mathbf{Y}_j \right]^2, \quad (91)$$

where p_j is a binary variable containing 1 or 0 according to the influence of each mode j (also row j) in the dynamics. For example, in planar motion (surge, heave and pitch), it is valid $p_1 = p_3 = p_5 = 1$ and $p_2 = p_4 = p_6 = 0$. Consequently, the model is fitted for this restricted motion.

6.6. Application of the algorithm

The algorithm is tested using the semisubmersible floating platform OE system (see Fig. 9). The main longitude is the structure length $L_0 = 170$ [m]. This system is very complex from a hydrodynamic viewpoint because the wet hull is very irregular in comparison with other systems like buoys, barges and ships. In consequence, the approximation order that is selected must be relatively large. In the implementation, the settings correspond to a motion of 6 degrees of freedom, i.e., $p_j = 1$, $L_j \in [1,\ 200]$ and $n = 6$. One notices in Figs. 21–24 that the fitting captures the largest resonance peaks reasonably well for the adopted order.

It is worth noticing that applications based on the state-space model of Jiang require low computational costs in comparison with the convolution model. Even when this advantage is shaded by the difficulties of selection of a suitable approximation order and finding stable models at the same time, it becomes more interesting when an analytical model is required. In applications concerning a low or limited range of frequencies or when the dynamics is only required in stationary state, a state-space model of low order is preferable, for example $n = 2$ or 3. On the contrary, when the hydrodynamics is so complex, a large order of approximation is necessary. But in this case, it may cause model instability.

7. Comparison of existing approaches

In this section, one summarises the features relative of the existing approaches seen earlier (see Table 1). Therein potential advantages are signalised with the symbol "$\surd$". It is noticed that stability and accuracy are the advantages of the convolution model, in contrast with the low computational costs and analyticity feature of the space-state model, which are the benefits of this approach.

In the following, a new state-space model is developed, which possesses a better stability and uniform accuracy for all elements like the convolution model, but keeps the analytical and computational advantages of the state-space model of Jiang.

8. New state-space model

From (63) and (64) consider the complex function matrix of the hydrodynamics for the regular part $\mathbf{s}_0$

$$H(\mathrm{j}\omega) = [-D(\omega) - \mathrm{j}\omega(M_\mathrm{a}(\omega) - M_\infty)], \tag{92}$$

whose real and imaginary components satisfy the extreme conditions

$$D(0) = 0 \tag{93}$$

$$D(\infty) = 0 \tag{94}$$

$$\lim_{\omega\to 0} \omega(M_\mathrm{a}(\omega) - M_\infty) = 0 \tag{95}$$

$$\lim_{\omega\to \infty} \omega(M_\mathrm{a}(\omega) - M_\infty) = 0. \tag{96}$$

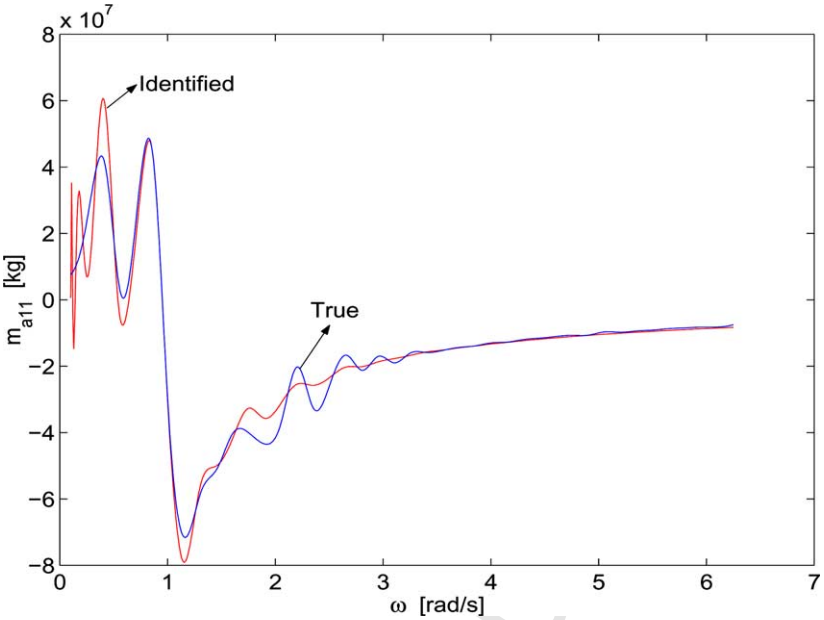

Fig. 21. Identification of the element $m_{a_{11}}(\omega)$ of the semisubmersible platform OE system.

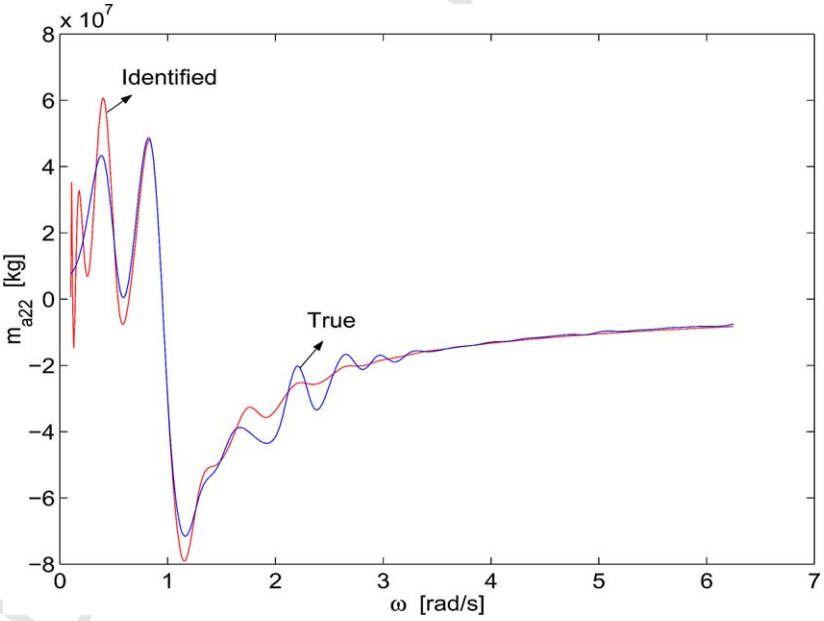

Fig. 22. Identification of the element $m_{a_{22}}(\omega)$ of the semisubmersible platform OE system.

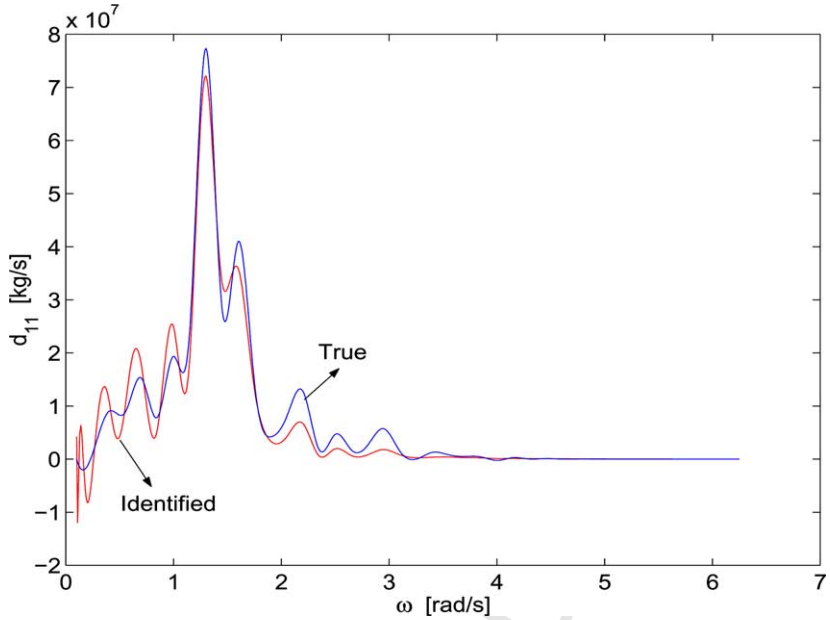

Fig. 23. Identification of the element $d_{11}(\omega)$ of the semisubmersible platform OE system.

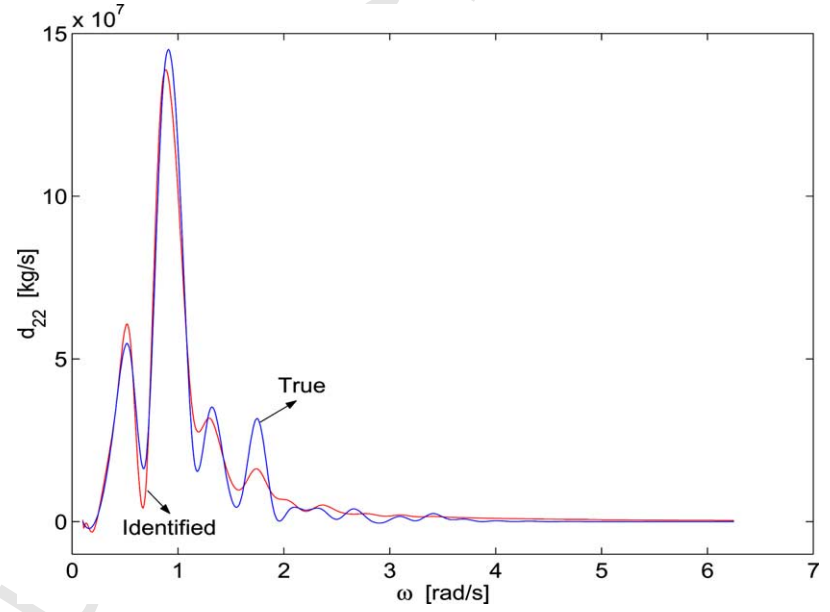

Fig. 24. Identification of the element $d_{22}(\omega)$ of the semisubmersible platform OE system.

Table 1
Feature comparison in the identification of the two model approaches

Convolution-based model	Space-state model
√ Inherent model stability	Model stability must be checked out during the optimal identification
√ Parameter: density of points per time unit of the time response	Parameter: approximation order n. Trade-off between accuracy and stability
√ Accuracy is uniformly distributed in the elements of the time response	Accuracy is optimised row by row in A_l and B_l. It is better for the largest element of the row
High memory need	√ Low memory need
High computational need	√ Low computational need
√ No restriction	Number of frequencies $N_\omega \geq (n+1)$
Convenient for dynamics analysis in only numerical form	√ Convenient for dynamic analysis in analytical and numerical form

Using the Initial Value Theorem of the Fourier Transform, we also point out the physical fact

$$K(0) = \lim_{\omega\to\infty} \frac{2}{\pi} \int_0^\infty D(\omega)\cos(\omega t)\,\mathrm{d}\omega \neq 0, \tag{97}$$

i.e., a sudden response of the system. Analogously, from the Final Value Theorem of the Fourier Transform one achieves

$$K(\infty) = \lim_{\omega\to 0} \frac{2\omega}{\pi} \int_0^\infty D(\omega)\,\mathrm{d}\omega = 0. \tag{98}$$

Conditions (93)–(94) obey the physical facts. Eq. (95) can be explained because $M_a(0)$ and M_∞ are finite matrix quantities. Condition (96) is accounted for from the Kramers–Kronig relationships (Bracewell, 1978) with the fact that $K(\tau)$ is continuous in τ, through (49), i.e.,

$$\lim_{\omega\to\infty} \omega(M_a(\omega) - M_\infty) \tag{99}$$

$$= \lim_{\omega\to\infty} \frac{-2}{\pi} \int_0^\infty \left(\int_0^\infty D(\omega)\cos(\omega t)\,\mathrm{d}\omega \right) \sin(\omega t)\,\mathrm{d}t \tag{100}$$

$$= \lim_{\omega\to\infty} \int_0^\infty K(t)\sin(\omega t)\,\mathrm{d}t \tag{101}$$

$$= 0. \tag{102}$$

Thus (92) can be approximated by a frequency transfer function matrix under the six conditions (93)–(98)

$$G(\mathrm{j}\omega) = \begin{bmatrix} \dfrac{P_{xx}(\mathrm{j}\omega)}{Q_{xx}(\mathrm{j}\omega)} & \dfrac{P_{xy}(\mathrm{j}\omega)}{Q_{xy}(\mathrm{j}\omega)} & \cdots & \dfrac{P_{x\psi}(\mathrm{j}\omega)}{Q_{x\psi}(\mathrm{j}\omega)} \\ \dfrac{P_{yx}(\mathrm{j}\omega)}{Q_{yx}(\mathrm{j}\omega)} & \dfrac{P_{yy}(\mathrm{j}\omega)}{Q_{yy}(\mathrm{j}\omega)} & \cdots & \dfrac{P_{y\psi}(\mathrm{j}\omega)}{Q_{y\psi}(\mathrm{j}\omega)} \\ \vdots & \vdots & \ddots & \vdots \\ \dfrac{P_{\psi x}(\mathrm{j}\omega)}{Q_{\psi x}(\mathrm{j}\omega)} & \dfrac{P_{\psi y}(\mathrm{j}\omega)}{Q_{\psi y}(\mathrm{j}\omega)} & \cdots & \dfrac{P_{\psi\psi}(\mathrm{j}\omega)}{Q_{\psi\psi}(\mathrm{j}\omega)} \end{bmatrix} \tag{103}$$

with zeros at $\omega = 0$ and $\omega = \infty$ due to (93)–(96). Consequently, every element of (103) must be a strictly proper rational function (conditions (94)–(96)) of order n with a single zero at $\omega = 0$ (conditions (93)–(95)) and n stable poles (98). Moreover, due to (97), every element of (103) must also have a relative degree equal one, i.e., $\mathrm{order}(Q_{jk}(\mathrm{j}\omega)) = \mathrm{order}(P_{jk}(\mathrm{j}\omega)) + 1$.

Accordingly, the Laplace transfer function element h_{jk} of (92) is

$$\frac{P_{jk}(s)}{Q_{jk}(s)} = \frac{s\left(b_{n-1}s^{n-2} + b_2 s + b_1\right)}{s^n + a_{n-1}s^{n-1} + \cdots + a_1 s + a_0}, \tag{104}$$

with s being the Laplace variable. In contrast with the space-state model of Jiang, the order n of the approximation may be different for each element in (103).

Corresponding to (103), the hydrodynamics is approximated alternative to (67) by

$$\mathbf{s}_0 = G(\mathrm{j}\omega)\dot{\mathbf{q}}, \tag{105}$$

and there exists the following class of minimal state-space representation

$$\begin{aligned} \dot{\mathbf{s}}_x &= A_x\mathbf{s}_x + B_x\dot{\mathbf{q}} \\ \dot{\mathbf{s}}_y &= A_y\mathbf{s}_y + B_y\dot{\mathbf{q}} \\ \dot{\mathbf{s}}_z &= A_z\mathbf{s}_z + B_z\dot{\mathbf{q}} \\ \dot{\mathbf{s}}_\varphi &= A_\varphi\mathbf{s}_\varphi + B_\varphi\dot{\mathbf{q}} \\ \dot{\mathbf{s}}_\theta &= A_\theta\mathbf{s}_\theta + B_\theta\dot{\mathbf{q}} \\ \dot{\mathbf{s}}_\psi &= A_\psi\mathbf{s}_\psi + B_\psi\dot{\mathbf{q}} \end{aligned}, \tag{106}$$

$$\mathbf{s}_0 = C^{\mathrm{T}}\left[\mathrm{s}_x, \ldots, \mathrm{s}_\psi\right], \tag{107}$$

where the new state vectors $\mathbf{s}_x, \ldots, \mathbf{s}_\psi$ have dimensions $\bar{n}_j = \sum_k n_{jk}$, with $j, k \in$

$\{x, y, z, \varphi, \theta, \psi\}$ and the matrices are

$$A_j = \begin{bmatrix} A_{jx} & 0 & 0 \\ 0 & \ddots & 0 \\ 0 & 0 & A_{j\psi} \end{bmatrix} \tag{108}$$

$$B_j = \operatorname{diag}\left(\begin{bmatrix} b_{xx_{n_{jx}-1}} & \dots & b_{x\psi_{n_{j\psi}-1}} \\ \vdots & \ddots & \vdots \\ b_{xx_1} & \dots & b_{x\psi_1} \\ 0 & \dots & 0 \end{bmatrix}, \dots, \begin{bmatrix} b_{\psi x_{n_{jx}-1}} & \dots & b_{\psi\psi_{n_{j\psi}-1}} \\ \vdots & \ddots & \vdots \\ b_{\psi x_1} & \dots & b_{\psi\psi_1} \\ 0 & \dots & 0 \end{bmatrix} \right), \tag{109}$$

$$C^{\mathrm{T}} = \begin{bmatrix} 0 & 0 & \dots & 1 \\ \vdots & \vdots & \ddots & \vdots \\ 0 & 0 & \dots & 1 \end{bmatrix}, \tag{110}$$

with the block matrices in the form

$$A_{jk} = \begin{bmatrix} -a_{jk_{n_{jk}-1}} & 1 & 0 & \dots & 0 \\ -a_{jk_{n_{jk}-2}} & 0 & 1 & \ddots & \vdots \\ \vdots & \vdots & 0 & \ddots & 0 \\ \vdots & \vdots & \vdots & \ddots & 1 \\ -a_{jk_0} & 0 & \dots & \dots & 0 \end{bmatrix}. \tag{111}$$

The matrix A_j represents the contribution of all mode motions for inducing the radiation load component of the mode j.

8.1. Stability

It is worth mentioning that the stability of the whole system (106) is established by the properties of the $\bar{n}$ eigenvalues λ_i to be

$$\operatorname{Re}\{\lambda_i(sI - A)\} < 0, \quad i = 1, \dots, \bar{n}, \tag{112}$$

with $\bar{n} = \sum_j \bar{n}_j = \sum_{j,k} n_{jk}$ and

$$A = \operatorname{diag}\{A_x, A_y, A_z, A_\varphi, A_\theta, A_\psi\}. \tag{113}$$

The state-space model (106)–(107) was expressed in the observable form. However, it can be transformed in every other usual canonical form.

One important advantage of this model is that the order n_{jk} of every transfer function (104) can be fitted for every complex function element of $H(\mathrm{j}\omega)$ independent of the others. On one side, this will lead to a saving in the number of coefficients in comparison with the first state-space representation. Additionally, it enables a better control of the stability in over-dimensioned approximations, which may become critical when unstable zero-pole cancellations occur.

8.2. Identification

The objective here is to develop an algorithm for parameter identification with rational model structures that reflect properties (93)–(96) in the state-space form (106), starting from frequency complex function matrices $M_{\mathrm{a}}(\omega)$ and $D(\omega)$.

The identification in frequency domain is usually difficult because it becomes ill-conditioned for relative larger orders n_{jk}. The reason for that is the construction of linear regressions that are commonly composed of monomial terms with different order of magnitudes in the frequency.

First, we note that $G(\mathrm{j}\omega)$ inherits the properties of symmetries of $H(\mathrm{j}\omega)$, i.e., it contains mostly 21 nonzero function elements. So the identification can be focused on elements on and over the diagonal (or under the diagonal).

Let us consider the element jk of $H(\mathrm{j}\omega)$ in the form (104), thus

$$-d_{jk}(\omega) - \mathrm{j}\omega\big(m_{\mathrm{a}_{jk}}(\omega) - m_{\infty_{jk}}\big) = P_{jk}(\mathrm{j}\omega)/Q_{jk}(\mathrm{j}\omega), \tag{114}$$

which leads after some transformations to

$$\begin{aligned} -d_{jk}(\omega) - \mathrm{j}\omega\bar{m}_{\mathrm{a}_{jk}}(\omega) = {} & \frac{1}{(\mathrm{j}\omega)^n} a_0 d_{jk}(\omega) + \frac{1}{(\mathrm{j}\omega)^{n-1}} \\ & \times \big(b_1 + a_1 d_{jk}(\omega) + a_0 \bar{m}_{\mathrm{a}_{jk}}(\omega)\big) + \cdots + \frac{1}{\mathrm{j}\omega} \\ & \times \big(b_{n-1} + a_{n-1} d_{jk}(\omega) + a_{n-2}\bar{m}_{\mathrm{a}_{jk}}(\omega)\big) \\ & + a_{n-1}\bar{m}_{\mathrm{a}_{jk}}(\omega), \end{aligned}$$

with $\bar{m}_{\mathrm{a}_{jk}} = m_{\mathrm{a}_{jk}} - m_{\infty_{jk}}$. Assuming n_{jk} even (the case with n_{jk} odd results analogously) one gets the regressor function

$$\begin{bmatrix} \phi_{\mathrm{real}}(\omega) \\ \phi_{\mathrm{imag}}(\omega) \end{bmatrix} = \begin{bmatrix} 0 & \frac{1}{(\mathrm{j}\omega)^{n-2}} \cdots \frac{-1}{\omega^2} 0 & \frac{1}{(\mathrm{j}\omega)^n} d_{jk}(\omega) & \frac{1}{(\mathrm{j}\omega)^{n-2}} \bar{m}_{\mathrm{a}_{jk}}(\omega) \ldots \frac{-1}{\omega^2} d_{jk}(\omega) & \bar{m}_{\mathrm{a}_{jk}}(\omega) \\ \frac{-1}{\mathrm{j}^{n-2}\omega^{n-1}} 0 & \ldots 0 \quad \frac{-1}{\omega} & \frac{-1}{\mathrm{j}^{n-2}\omega^{n-1}} \bar{m}_{\mathrm{a}_{jk}}(\omega) & \frac{-1}{\mathrm{j}^{n-2}\omega^{n-1}} d_{jk}(\omega) \ldots \frac{-1}{\omega} \bar{m}_{\mathrm{a}_{jk}}(\omega) & \frac{-1}{\omega} d_{jk}(\omega) \end{bmatrix}, \tag{116}$$

so that it accomplishes the linear regression function

$$\begin{bmatrix} -d_{jk}(\omega) \\ -\omega\bar{m}_{\mathrm{a}_{jk}}(\omega) \end{bmatrix} = \begin{bmatrix} \phi_{\mathrm{real}_{jk}}(\omega) \\ \phi_{\mathrm{imag}_{jk}}(\omega) \end{bmatrix} \theta_{jk}, \tag{117}$$

with the unknowns arrayed in the parameter vector

$$\theta_{jk} = [b_1\, b_2 \ldots b_{n-1}\, a_0\, a_1 \ldots a_{n-1}]^{\mathrm{T}}. \tag{118}$$

An estimation of θ_{jk} using norm two is preferred because of mathematical advantages. So we can directly apply the least-squares method (LS) in frequency domain. Besides, a discrete identification method can be employed.

Toward this goal, let the so-called data matrix be constructed through (116) onto a frequency-discrete domain of N_ω frequencies as

$$\Psi_{jk}(\omega) = \begin{bmatrix} \phi_{\text{real}_{jk}}(\omega_1) \\ \phi_{\text{imag}_{jk}}(\omega_1) \\ \phi_{\text{real}_{jk}}(\omega_2) \\ \phi_{\text{imag}_{jk}}(\omega_2) \\ \vdots \\ \phi_{\text{real}_{jk}}(\omega_{N_\omega}) \\ \phi_{\text{imag}_{jk}}(\omega_{N_\omega}) \end{bmatrix}, \tag{119}$$

Similarly, let the so-called data vector be defined for the same set of frequencies as

$$\mathbf{Y}_{jk}(\omega) = \begin{bmatrix} -d_{jk}(\omega_1) \\ -\omega\bar{m}_{jk}(\omega_1) \\ -d_{jk}(\omega_2) \\ -\omega\bar{m}_{jk}(\omega_2) \\ \vdots \\ -d_{jk}(\omega_{N_\omega}) \\ -\omega\bar{m}_{jk}(\omega_{N_\omega}) \end{bmatrix}. \tag{120}$$

Previous to developing an estimation method, let us point out the numerical problem that arises when regressor function (116) is evaluated at small frequencies. In this case, the first columns of (116) are numerically larger in many orders of magnitude than the last ones. On the contrary, when the frequency is large, the first columns of (116) are numerically smaller in many orders of magnitude than the last ones. This fact has negative consequences in the LS solution because the so-called pseudoinverse of the LS algorithm given $[\Psi_{jk}^{\mathrm{T}}\Psi_{jk}]^{-1}$ results in general ill-conditioned.

8.3. Optimal estimation

One manner to circumvent this problem consists in using a weighted norm, which attains the optimal LS estimation by accomplishing the restriction

$$\frac{\partial\left[\left(\mathbf{Y}_{jk}(\omega) - \Psi_{jk}(\omega)\theta_{jk}\right)^{\mathrm{T}} W(\omega)\left(\mathbf{Y}_{jk}(\omega) - \Psi_{jk}(\omega)\theta_{jk}\right)\right]}{\partial\theta_{jk}} = 0, \tag{121}$$

with the function in brackets containing the sum of weighted quadratic errors for the N_ω samples. The matrix W is a weighting matrix. The solution of (121) is

$$\theta_{jk_{\text{opt}}} = \left[\Psi_{jk}^{\mathrm{T}}(\omega) W(\omega) \Psi_{jk}(\omega)\right]^{-1} \Psi_{jk}^{\mathrm{T}}(\omega) W(\omega) \mathbf{Y}_{jk}(\omega). \tag{122}$$

We propose a particular function matrix W in the frequency so that it would be possible to get a better conditioned pseudoinverse of the weighted LS problem. If

W is chosen diagonal such as

$$W(\omega) = \mathrm{diag}(f_1(\omega_1), f_2(\omega_1), \ldots, f_1(\omega_{N_\omega}), f_2(\omega_{N_\omega})), \tag{123}$$

where $f_1(\omega)$ and $f_2(\omega)$ are some weighting functions, then the columns of $W(\omega)\Psi_{jk}(\omega)$ can be influenced in such a way that the linear independence among them can be strengthened.

The way we do that consists in selecting weighting functions

$$f_1(\omega) = \omega^{\gamma_1}, \quad \text{with } \gamma_1 > 0, \tag{124}$$

$$f_2(\omega) = \omega^{\gamma_2}, \quad \text{with } \gamma_2 > 0, \tag{125}$$

such that the numerically rounded vectors $\phi_{\mathrm{real}_{jk}}$ and $\phi_{\mathrm{imag}_{jk}}$ satisfy

$$\max_{\gamma_1 \in \Re^1_+} \det\left[\frac{1}{\omega}\int_0^\omega \omega^{2\gamma_1}\phi^{\mathrm{T}}_{\mathrm{real}_{jk}}(\omega)\phi_{\mathrm{real}_{jk}}(\omega)\,\mathrm{d}\omega\right] = \alpha_1 > 0, \tag{126}$$

$$\max_{\gamma_2 \in \Re^1_+} \det\left[\frac{1}{\omega}\int_0^\omega \omega^{2\gamma_2}\phi^{\mathrm{T}}_{\mathrm{imag}_{jk}}(\omega)\phi_{\mathrm{imag}_{jk}}(\omega)\,\mathrm{d}\omega\right] = \alpha_2 > 0, \tag{127}$$

i.e., $\omega^{\gamma_1}\phi_{\mathrm{real}_{jk}}(\omega)$ and $\omega^{\gamma_2}\phi_{\mathrm{imag}_{jk}}(\omega)$ both span spaces of dimension equal to $\dim(\theta_{jk})$ with maximal levels α_1 and α_2, respectively. Hence the data regressor (116) becomes

$$\begin{bmatrix}\omega^{\gamma_1}\phi_{\mathrm{real}}(\omega)\\ \omega^{\gamma_2}\phi_{\mathrm{imag}}(\omega)\end{bmatrix} = \begin{bmatrix} 0 & \frac{1}{\mathrm{j}^{n-2}(\omega)^{n-2-\gamma_1}} & \cdots & \frac{-1}{\omega^2-\gamma_1} & 0 & \frac{1}{\mathrm{j}^n(\omega)^{n-\gamma_1}}d_{jk}(\omega) & \frac{1}{\mathrm{j}^{n-2}(\omega)^{n-2-\gamma_1}}\bar{m}_{jk}(\omega) & \cdots & \frac{-1}{\omega^{2-\gamma_1}}d_{jk}(\omega) & \frac{1}{\omega^{-\gamma_1}}\bar{m}_{jk}(\omega)\\ \frac{1}{\mathrm{j}^{n-2}\omega^{n-1-\gamma_2}} & 0 & \cdots & 0 & \frac{-1}{\omega^2-\gamma_2} & \frac{-1}{\mathrm{j}^{n-2}\omega^{n-1-\gamma_2}}\bar{m}_{jk}(\omega) & \frac{1}{\mathrm{j}^{n-2}\omega^{n-1-\gamma_2}}d_{jk}(\omega) & \cdots & \frac{-1}{\omega^{1-\gamma_2}}\bar{m}_{jk}(\omega) & \frac{-1}{\omega^{1-\gamma_2}}d_{jk}(\omega)\end{bmatrix}. \tag{128}$$

It can be seen in the equation above that properly selected functions ω^{γ_1} and ω^{γ_2} have the effect of flattening the order of magnitudes of the columns of ϕ_{real} and ϕ_{imag} in every frequency. This will substantially better the solution from a numerical viewpoint, especially for large orders of the rational transfer function model (104). Since the exponents of the elements of $\omega^{\gamma_1}\phi_{\mathrm{real}}$ and $\omega^{\gamma_2}\phi_{\mathrm{imag}}$ are similar in the order of magnitude, we simply choose $\gamma_1 = \gamma_2 = \gamma$. Fig. 25 shows the weighting function ω^γ parameterised in γ.

An optimal gain γ can be analytically be found by establishing the following optimal criterion on the sum of weighted LS errors

$$\begin{aligned}\min_{\gamma\in\Re^1_+} E_{jk}(\gamma) &= \min_{\gamma\in\Re^1_+}\left(\mathbf{Y}_{jk} - \Psi^{\mathrm{T}}_{jk}\theta_{jk_{\mathrm{opt}}}\right)^{\mathrm{T}} W(\gamma)\left(\mathbf{Y}_{jk} - \Psi_{jk}\theta_{jk_{\mathrm{opt}}}\right)\\ &= \min_{\gamma\in\Re^1_+}\left(\mathbf{Y}_{jk} - \Psi_{jk}\left[\Psi^{\mathrm{T}}_{jk}W(\gamma)\Psi_{jk}\right]^{-1}\Psi^{\mathrm{T}}_{jk}W(\gamma)\mathbf{Y}_{jk}\right)^{\mathrm{T}}\\ &\quad\times W(\gamma)\left(\mathbf{Y}_{jk} - \Psi_{jk}\left[\Psi^{\mathrm{T}}_{jk}W(\gamma)\Psi_{jk}\right]^{-1}\Psi^{\mathrm{T}}_{jk}W(\gamma)\mathbf{Y}_{jk}\right),\end{aligned} \tag{129}$$

and then making $\partial E_{jk}(\gamma)/\partial\gamma = 0$ in order to pick up the optimal γ.

Similar to the optimal estimation of the model (67), this solution does not ensure model stability. Hence, instead of following this way, we will involve the problem

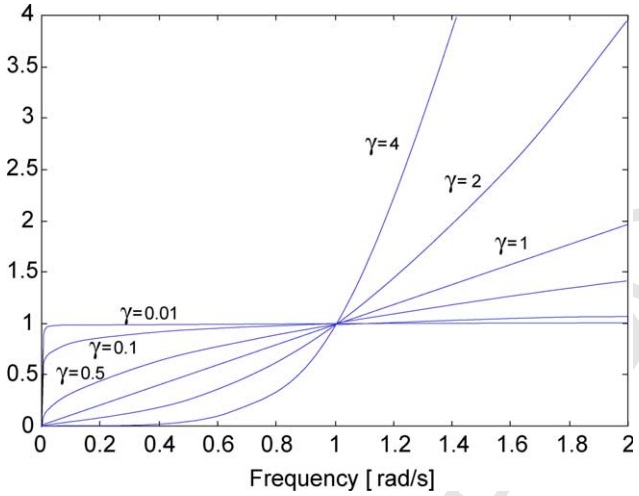

Fig. 25. Weighting function for optimal estimation.

of instability of the model in the estimation of rational transfer functions in frequency domain.

8.4. Suboptimal estimation

The stability of the model is ensured when the system matrix (113) does satisfy (112). As it may not occur for the optimal value of γ, a suboptimal solution is generally chosen instead. The criterion for obtaining this solution consists in a constrained optimisation of the sum of the LS errors

$$\min_{\gamma\in\Re_+^1 \mathrm{Re}\{\lambda_i(Q_{jk}(s)=0)\}<0} E_{jk}(\gamma) = \min_{\gamma\in\Re_+^1 \mathrm{Re}\{\lambda_i(Q_{jk}(s)=0)\}<0} \left[\mathbf{Y}_{jk}^{\mathrm{T}} W(\gamma)\mathbf{Y}_{jk} - 2\mathbf{Y}_{jk}^{\mathrm{T}}\Lambda_{jk}^{\mathrm{T}}\mathbf{Y}_{jk} + \mathbf{Y}_{jk}^{\mathrm{T}}\Lambda_{jk}^{\mathrm{T}}\Lambda_{jk}\mathbf{Y}_{jk}\right], \quad (130)$$

with $\Lambda_{jk} = W(\gamma)\ \Psi_{jk}[\Psi_{jk}^{\mathrm{T}} W(\gamma)\Psi_{jk}]^{-1}\Psi_{jk}^{\mathrm{T}} W(\gamma)$ and $Q_{jk}(s) = 0$ the characteristic equation related to the transfer function $P_{jk}(s)/Q_{jk}(s)$. This concludes the estimation of one transfer function.

8.5. Filtering in frequency domain

One notices from Figs. 10 to 17 that the hydrodynamic complex function components $d_{jk}(\omega)$ and $m_{jk}(\omega)$ possess in general many resonance peaks. These can be accounted for from physical reasons. When the wet surface has a changing radius of curvature, the potential damping and the added mass look fluctuating in the frequency domain (for instance, in a semisubmersible). On the contrary, if the radius of curvature is constant as in a spherical buoy, the frequency responses for potential damping and added mass are smooth.

The consequence is that the more irregular is the geometry of the wet surface, the larger must be the order of the model chosen and vice versa. As the identification is carried out systematically element by element, the corresponding order n_{jk} is chosen individually according to the number of resonance peaks of the function $d_{jk}(\omega)$ or $m_{jk}(\omega)$. The following general rule can be applied as reference

$$n_{jk} \geq 2 \times \text{number of resonance peaks of } d_{jk}(\omega). \tag{131}$$

When the dynamics of a complex OE system is excited in a narrow interval of frequency, the selection of a large model order may make no sense. It is then more appropriate to chose a reduce-order model for this application interval of frequency. A suitable way to fit the model response to a small frequency interval is to employ a smooth filter like

$$p(\omega; \omega_{c_\infty}, m, \beta) = e^{-\beta(\omega/\omega_{c_\infty})m}, \tag{132}$$

where ω_{c_∞} is the cut frequency of the filter for $m = \infty$, m the filter order with $m \geq 2$ and even, and $\beta > 0$ the filter coefficient.

The smooth filter has the properties (see Figs. 26 and 27)

$$\lim_{m\to\infty} p(\omega; \omega_{c_\infty}, m, \beta) = \begin{cases} 1 \text{ for } \omega < \omega_{c_\infty} \\ 0 \text{ for } \omega \geq \omega_{c_\infty} \end{cases} \tag{133}$$

$$\lim_{\beta\to 0} p(\omega; \omega_{c_\infty}, m, \beta) = 1 \tag{134}$$

$$\lim_{\beta\to\infty} p(\omega; \omega_{c_\infty}, m, \beta) = 0. \tag{135}$$

So, the filter applies to the potential-damping function element and one achieves

$$\bar{d}_{jk}(\omega) = e^{-\beta(\omega/\omega_{c_\infty})m} d_{jk}(\omega), \tag{136}$$

with $\bar{d}_{jk}$ a filtered element function to be employed in the regression (117) instead of d_{jk}.

Let us exemplify in Fig. 28 the application of (132) to a potential-damping function element of a semisubmersible for different β's. It is shown that the filtered damping functions drop down abruptly for different particular β's. However, in the pass-band of frequencies, the course of the functions remain practically intact with respect to the true function. The reason for that is the selection of a high-order filter for this application. It is also noticed that for large values of m, the cut frequency for $\bar{d}_{11}(\omega)$ can be alternatively defined by a proper selection of β with $\omega_{c_\infty} = 1$.

The same filter process could also be accomplished for the added-mass function $(m_{jk}(\omega) - m_{\infty_{jk}})$. But doing that, the Kramers–Kronig relations are no longer valid since

$$e^{-\beta(\omega/\omega_{c_\infty})m}\left[\omega\left(m_{jk}(\omega) - m_{\infty_{jk}}\right)\right] \neq \frac{-2}{\pi}\int_0^\infty \left[\int_0^\infty e^{-\beta(\omega/\omega_{c_\infty})^m} d_{jk}(\omega)\cos(\omega t)\, d\omega\right]\sin(\omega t)\, dt. \tag{137}$$

The equality in (137) would be only valid in the case $\beta = 0$ (see property (134)).

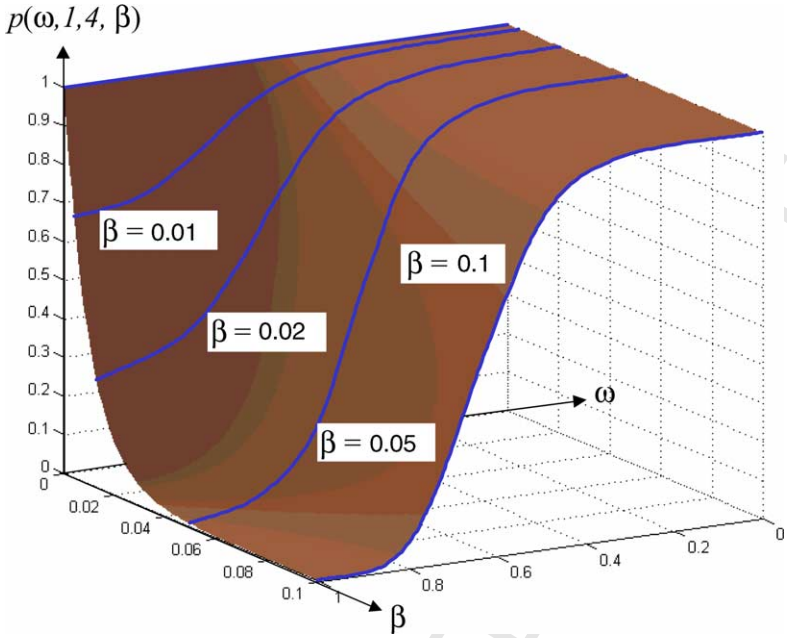

Fig. 26. Smooth filter in ω and β domains, for $m = 4$ and $\omega_{c_\infty} = 1$.

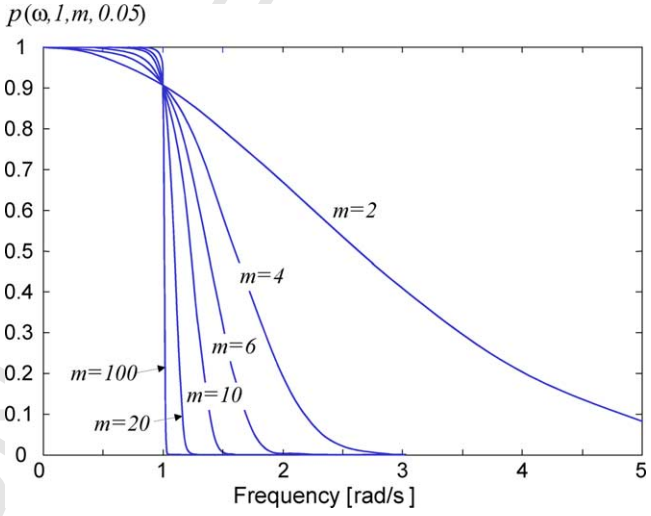

Fig. 27. Smooth filter for different orders m's, with $\beta = 0.05$ and $\omega_{c_\infty} = 1$.

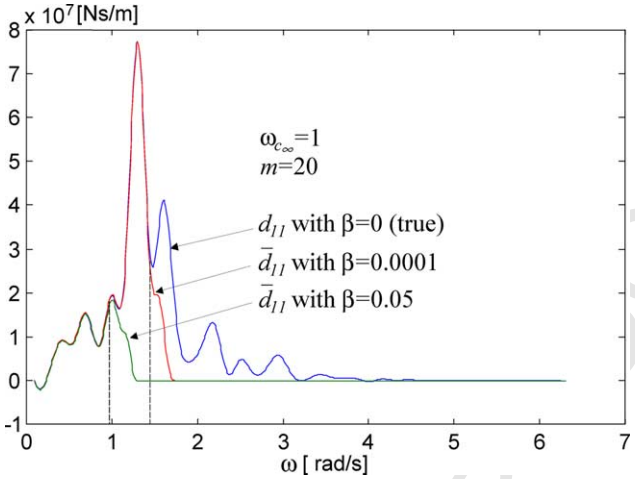

Fig. 28. Filtered induced-radiation damping function $d_{11}(\omega)$ of a semisubmersible for three different β's.

So, for the identification we use instead the filtered added mass as achieved by

$$\overline{m_{jk}(\omega) - m_{\infty_{jk}}} = \frac{-2}{\omega\pi}\int_0^\infty \left[\int_0^\infty \bar{d}_{jk}(\omega)\cos(\omega t)\,\mathrm{d}\omega\right]\sin(\omega t)\,\mathrm{d}t. \tag{138}$$

Thus the filtered transfer function element h_{jk} of (92) is

$$\bar{h}_{jk} = \mathrm{e}^{-\beta(\omega/\omega_{c_\infty})^m} h_{jk}, \tag{139}$$

$$= -\bar{d}_{jk}(\omega) - \mathrm{j}\omega\overline{m_{jk}(\omega) - m_{\infty_{jk}}}. \tag{140}$$

Clearly the new filtered component (139)–(140) satisfies the Kramers–Kronig relation.

In the following, the filtering process is incorporated to the algorithm when a reduced-order model is desired.

8.6. Sample density

Since the transfer function model (92) as well as the state-space model (106) continues in frequency and time, respectively, the identification through frequency-discrete samples reduces the precision of the model attained. If the set of samples N_ω is small, then a high-order interpolation of the samples is necessary in order to increase N_ω.

For this purpose, a cubic spline data interpolation is introduced as described in Section 4.3. This involves the damping function first.

Once the reconstructed function $\bar{d}_{jk}(\omega)$ is obtained, one can sample it regularly for the purpose of identification at a step

$$\Delta\omega = \frac{\omega_{\max} - \omega_{\min}}{\rho N_\omega}, \tag{141}$$

with $\omega_{\min}$, $\omega_{\max}$ being the minimum and maximum frequency in the domain interval, respectively, and ρ indicating the density of points with respect to the original set of samples $d_{jk}(\omega_i)$. So the set $\{\bar{d}_{jk}(\omega_i)\}_{i=1}^{\rho N_\omega}$ is obtained (in general $\rho > 1$).

Finally, the reconstructed added-mass functions result from the Kramers–Kronig relation

$$\bar{m}_{jk}(\omega) - m_\infty = \frac{-2}{\omega\pi}\int_0^\infty \left[\int_0^\infty \bar{d}_{jk}(\omega)\cos(\omega t)\,\mathrm{d}\omega\right]\sin(\omega t)\,\mathrm{d}t, \tag{142}$$

with the posterior sample of $\bar{m}_{jk}$ at the rate ρ to give $\{\bar{m}_{jk}(\omega_i) - m_{\infty_{jk}}\}_{i=1}^{\rho N_\omega}$. Note that the integrals in (142) are performed piecewise for every neighbouring interval $[\omega_i, \omega_{i+1}]$.

8.7. Complete description of the estimation algorithm

The parameter estimation algorithm for the state-space model (106) can be characterised as a systematic process, in which all transfer function elements in the matrix $H(\mathrm{j}\omega)$ of (92) are identified one by one till the whole matrix is completely scanned. Symmetries of $H(\mathrm{j}\omega)$ are taken into account in order to diminish the number of steps. The state-space model is finally conformed according to (108)–(109) from all the estimations of θ_{jk}'s.

The algorithm for optimal estimation is summarised in the following.

Step 1 Selection of one h_{jk} of (92).

Step 2 Selection of design parameters for h_{jk}.

Design parameter	Symbol
Order of the transfer function jk	n_{jk}
Filter order	m
Filter coefficient	β
Filter cut frequency for $m = \infty$	ω_{c_∞}
Interval for optimal estimation	$[\gamma_{\min}, \gamma_{\max}]$
Number of frequency samples	N_ω
Density of frequency samples in spline	ρ

Step 3 Reconstruction of the hydrodynamic coefficients in continuous frequency

$$d_{jk}(\omega) = \alpha_{jk}(\omega - \omega_i)^3 + \beta_{jk}(\omega - \omega_i)^2 + \gamma_{jk}(\omega - \omega_i) + \delta_{jk},$$

$$m_{jk}(\omega) - m_{\infty_{jk}} = \frac{-2}{\omega\pi}\int_0^\infty \left[\int_0^\infty d_{jk}(\omega)\cos(\omega t)\,\mathrm{d}\omega\right]\sin(\omega t)\,\mathrm{d}t.$$

Step 4 Smooth filtering

$$\bar{d}_{jk}(\omega) = \mathrm{e}^{-\beta(\omega/\omega_{c_\infty})^m} d_{jk}(\omega).$$

Step 5 Construction of discrete-frequency sets with density ρ

$$\{\bar{\boldsymbol{d}}_{jk}(\omega_i)\}_{i=1}^{\rho N_\omega},$$

$$\{\bar{\boldsymbol{m}}_{jk}(\omega_i) - m_{\infty_{jk}}\}_{i=1}^{\rho N_\omega}.$$

Step 6 Construction of the regressors $\mathbf{Y}_{jk}(\omega_i)$ and $\Psi_{jk}(\omega_i)$, and weighting function $W(\gamma_{\min})$

Step 7 Constrained optimisation according to (130) for obtaining θ_{jk}

$$\min_{\gamma\in|\gamma_{\min},\gamma_{\max}|\mathrm{Re}\{\lambda_i(Q_{jk}(s)=0)\}<0} E_{jk}(\gamma)$$

$$= \min_{\gamma\in|\gamma_{\min},\gamma_{\max}|\mathrm{Re}\{\lambda_i(Q_{jk}(s)=0)\}<0} \Big[\mathbf{Y}_{jk}^{\mathrm{T}} W(\gamma)\mathbf{Y}_{jk} - 2\mathbf{Y}_{jk}^{\mathrm{T}}\Lambda_{jk}^{\mathrm{T}}(\gamma)\mathbf{Y}_{jk} + \mathbf{Y}_{jk}^{\mathrm{T}}\Lambda_{jk}^{\mathrm{T}}(\gamma)\Lambda_{jk}(\gamma)\mathbf{Y}_{jk}\Big]$$

If the optimisation fails, i.e., no identified model becomes stable, one attempts with a lower order n_{jk} and repeats Step 6 and Step 7.

Step 8 Construction of the rational function model $P_{jk}(\mathrm{j}\omega)/Q_{jk}(\mathrm{j}\omega)$ upon the identified θ_{jk} from Step 7.

Step 9 Scanning of all elements h_{jk} of (92) on and upon the diagonal of $H(\mathrm{j}\omega)$ through Steps 1–8.

Step 10 Construction of the state-space model (106) through the matrices A_j and B_j.

8.8. Design parameter selection

In the following, some guidelines for the selection of design parameters in the table of Step 1 are given.

8.8.1. Selection of model order

As a rule of thumb, an acceptable identification of the whole frequency response of the hydrodynamic transfer functions $h_{jk}(\omega)$ can be assured by choosing n_{jk} according to the equality given in (131). However, complex geometries demand relatively large values of n_{jk} and then the advantages of a transfer function model are shaded by convolution models, which are more appropriate in these circumstances. Let us analyse some common situations where a reduced-order model would be reasonable.

Usually the forced steady state of moored OE systems is characterised by the presence of subharmonics. This nonlinear phenomenon is often caused by the nonlinear characteristics of the mooring lines which leads to system dynamics, whose ordinary differential equations can be described typically by Duffing's equation or Mathieu's equation (Landa, 2001; Guckenheimer and Holmes, 1997). In both cases, the appearance of subharmonics in the dynamics is characteristic for certain settings of the catenaries and of geometric and physical parameters. The fundamental frequency in the stationary dynamics are just the frequency of the wave.

The subharmonics as well as the most probable maximal fundamental frequency must be consequently in the pass-band of $h_{jk}(\omega)$.

On the other hand for irregular sea states, the energy of the wave is continuously spread in the frequency domain and statistically described by a density spectral function or spectrum. A well-studied wave spectrum is that of Pierson–Moskowitz (PM), developed for wind-generated seas from analyses of wave spectra in the North Atlantic Ocean. A glance at Fig. 29 shows that the significant interval where the wave energy statistically lies is constrained approximately from 0.35 up to 1 (rad/s). Hence, in stationary state with irregular waves given by the PM spectrum, the pass-band of the transfer functions $h_{jk}(\omega)$ cannot be larger than 1 (rad/s).

However, in transient states, a body with considerably low inertia can radiate a substantial energy in different frequencies, so the induced-radiation forces could be much more dominant than the incident waves of first order (Froude–Kryloff forces). However, the larger is the system inertia, the smaller will be the energy of high frequency components of the radiation forces. Therefore, in order to capture this transitory behaviour in a reliable form specially for low-inertia systems, the cut frequency for the hydrodynamic model must be at least greater than the largest resonance peak frequency of h_{jk} outside the significant wave frequency interval.

Concerning Fig. 28 related to a high-inertia platform, the order $n_{11} = 4$ or 6 could be satisfactory for the filtered function with $\beta = 0.05$. On the contrary, if the function was obtained with $\beta = 0.001$, the order would be selected $n_{11} = 6$ or 8 in order to capture the greater peak at $\omega = 1.2$ (rad/s). In both cases, the order $n_{11} = 6$ could be suitable for registering the dominant transient behaviour through an order-reduced model.

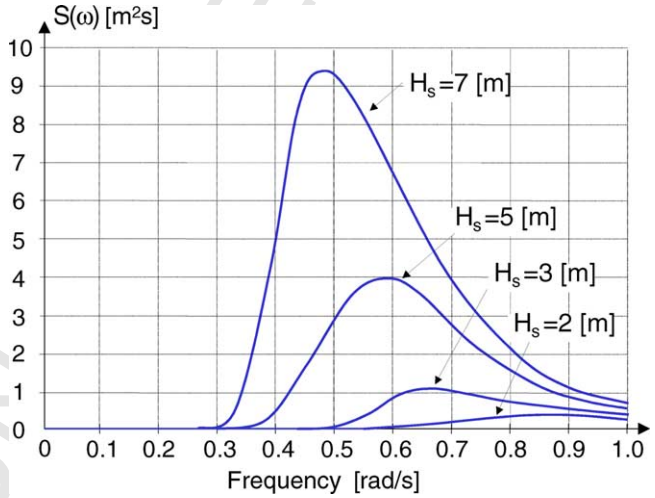

Fig. 29. Pierson–Moskowitz spectrum for different significant wave heights H_s.

8.8.2. Selection of filter parameters

All the filter parameters μ, β and ω_{c_∞} determine the number of resonance peaks entering in the pass-band of the significant dynamics. In particular, the setup is simplified by choosing m in a large dimension, say $m = 20$, $\omega_{c_\infty} = 1$ and β to be adjustable in order to accomplish an abrupt decay of the filter gain at a desired cut frequency.

8.8.3. Selection of interval for optimal estimation

A suitable choice of γ can improve the condition of the pseudoinverse in the parameter estimation. A look at (128) with $\gamma_1 = \gamma_2 = \gamma$ suggests that with $\gamma = 0$, there results a series of weights $\{\omega^{-n_{jk}}, \omega^{1-n_{jk}}, \ldots, \omega^0\}$, and with $\gamma = n_{jk}$ a series of weights $\{\omega^0, \omega^1, \ldots, \omega^{n_{jk}}\}$. So a reasonable interval for the optimal search in Step 7 would be

$$[\gamma_{\min}, \gamma_{\max}] = [0, n_{jk}]. \tag{143}$$

For performing the optimisation numerically, the partition of this interval can be simply regular.

8.8.4. Selection of number of frequency samples

Usually, the hydrodynamic coefficients are obtained by special ad hoc programs. Many available commercial versions of these programs are available. The user typically decides which frequencies will enter the series $\{d_{jk}(\omega_i)\}_{i=1}^{N_\omega}$ and $\{m_{jk}(\omega_i)\}_{i=1}^{N_\omega}$. What is important is that the resonance peaks are captured in such a selection. If the number of discrete frequencies is not large enough, then a smooth reconstruction is needed for, for instance, a cubic interpolation. A cubic reconstruction additionally serves to achieve an improvement in the numerical solution of the integrals involved in the Kramers–Kronig relations.

9. Case studies

In this section, the algorithm is tested with different geometries for the wet hull, namely, a spherical buoy (Fig. 30), a spar buoy (Fig. 2), and a semisubmersible floating platform (Fig. 9). Clearly, the complexity of the hydrodynamics increases for the most irregular surface, i.e., the semisubmersible, in comparison with the other OE systems. The consequence of this is that the orders for the transfer function approximations must be selected to be relatively large in comparison with the more simple case, i.e., the spherical buoy.

9.1. Case 1: spherical buoy

A semisubmerged spherical buoy meets all plane symmetries, namely in the xy-, xz- and yz-planes. Additionally, it possesses radial symmetry with respect to

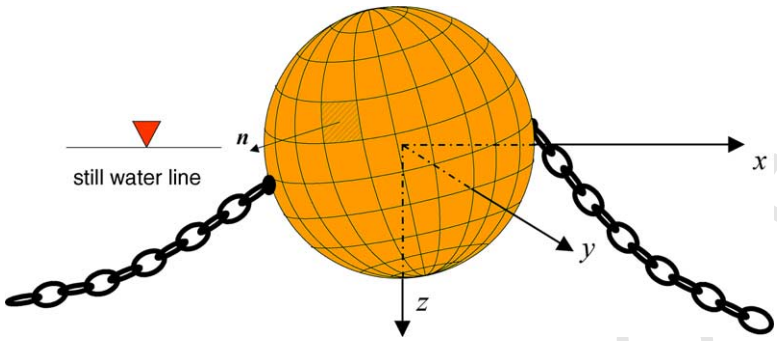

Fig. 30. Moored OE system semisubmerged spherical buoy.

every principal axis. Therefore, the hydrodynamics simplifies to

$$H(\mathrm{j}\omega) = \begin{bmatrix} h_{11} & 0 & 0 & 0 & 0 & 0 \\ 0 & h_{11} & 0 & 0 & 0 & 0 \\ 0 & 0 & h_{33} & 0 & 0 & 0 \\ 0 & 0 & 0 & 0 & 0 & 0 \\ 0 & 0 & 0 & 0 & 0 & 0 \\ 0 & 0 & 0 & 0 & 0 & 0 \end{bmatrix}, \tag{144}$$

with only two different elements.

As the radius of the wet hull is constant, one attempts to use a low order, for instance $n_{jk} = 2$. In Table 2, the design parameters for the optimal identification are described. They are uniformly selected for all elements h_{jk}.

When performing the constrained optimisation, the algorithm found all stable models with minimum LS error E_{jk} for $\gamma = \gamma_{\mathrm{opt}} = 0.01$, i.e., it took the minimum value $\gamma_{\min}$. Table 3 shows the identified transfer function elements corresponding to h_{11} and h_{33} for the order $n_{11} = n_{33} = 2$.

Figs. 31 and 32 show the real and imaginary parts of an estimated element. One notices that order six fits better than order two, but at the cost of increasing the number of coefficients significantly. Additionally, from Table 3 one notes that the element h_{33} is practically proportional to h_{11}, which is theoretically reasonable.

Table 2
Design parameters for identification of a spherical buoy

n_{jk}	2
M	4
β	0.001
ω_{c_∞}	1
N_ω	34
ρ	18
$[\gamma_{\min}, \gamma_{\max}]$	[0.01, 2]
$[\omega_{\min}, \omega_{\max}]$	[0.0125, 6.5]

Table 3
Rational transfer functions for the hydrodynamics of a spherical buoy

$H(s)$	$P_{jk}(s)$ with coefficients: b_2, b_1, b_0
	$Q_{jk}(s)$ with coefficients: a_2, a_1, a_0
$P_{11}(s)/Q_{11}(s)$	0, 2.4822×10^{-1}, 0
	1, 3.6095×10^{-1}, 9.8585×10^{-1}
$P_{33}(s)/Q_{33}(s)$	0, 4.6158×10^{-1}, 0
	1, 3.5011×10^{-1}, 9.8246×10^{-1}

9.2. Case 2: spar buoy

In a spar buoy, the xz- and yz-plane symmetries concur together (see Fig. 2). Moreover, it possesses radial symmetry with respect to the z-axis. As a consequence, the complex hydrodynamic matrix results in simplified

$$H(\mathrm{j}\omega) = \begin{bmatrix} h_{11} & 0 & h_{13} & 0 & h_{15} & 0 \\ 0 & h_{11} & 0 & h_{15} & 0 & 0 \\ h_{13} & 0 & h_{33} & 0 & 0 & 0 \\ 0 & h_{15} & 0 & h_{44} & 0 & 0 \\ h_{15} & 0 & 0 & 0 & h_{44} & 0 \\ 0 & 0 & 0 & 0 & 0 & 0 \end{bmatrix}, \tag{145}$$

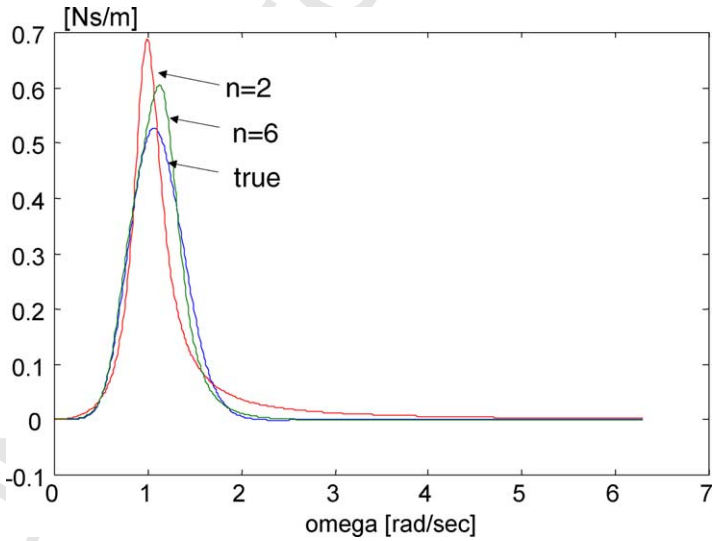

Fig. 31. Optimal estimation of the real part of $h_{11}(\mathrm{j}\omega)$ in a spherical buoy for different orders.

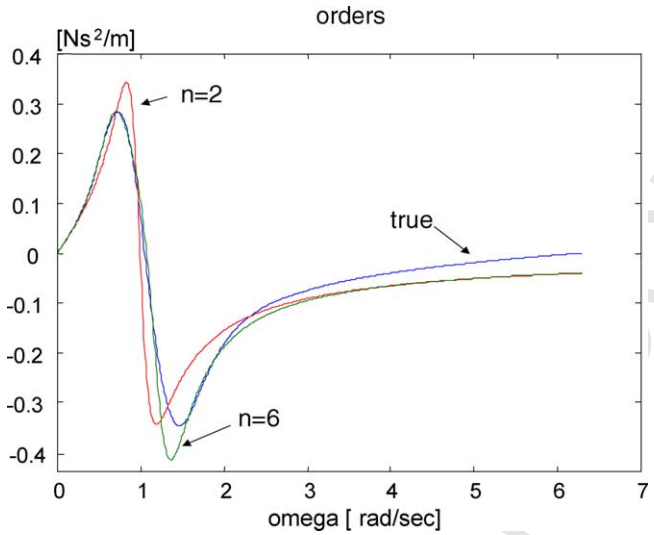

Fig. 32. Optimal estimation of the real part of $h_{11}(j\omega)$ in a spherical buoy for different orders.

with only five different elements. In Table 4, the setup for the identification is shown.

The estimation of $h_{15}(\omega)$ can be seen in Figs. 33 and 34 for $n_{jk} = 2$, $n_{jk} = 4$ and $n_{jk} = 6$. One infers that $n_{jk} = 4$ and $n_{jk} = 6$ practically bring the same all-round performance of the curve fitting. As this occurs approximately with all functions h_{jk}, one selects the lower model order $n_{jk} = 4$. Table 5 describes the rational transfer functions for $n_{jk} = 4$.

One pays attention to the fact that the weighting exponent γ takes optimal values within the search interval.

Table 4
Design parameters for identification of a spar buoy

n_{jk}	4
m	4
β	0.05
ω_{c_∞}	1
N_ω	37
ρ	34
$[\gamma_{\min}, \gamma_{\max}]$	[0.01, 2]
$[\omega_{\min}, \omega_{\max}]$	[0.00628, 12.5]

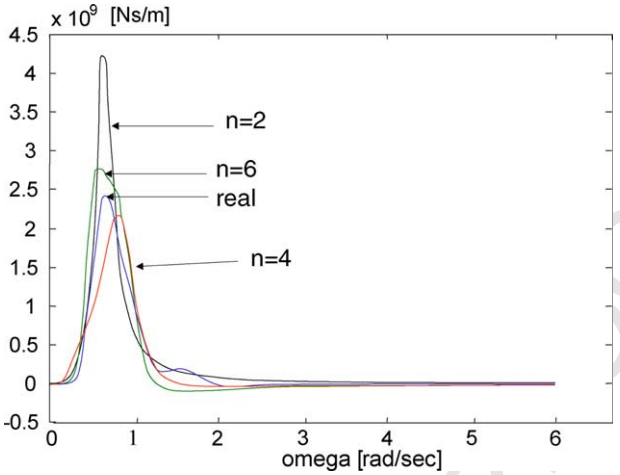

Fig. 33. Optimal estimation of the real part of $h_{15}(j\omega)$ in a spar buoy for different orders.

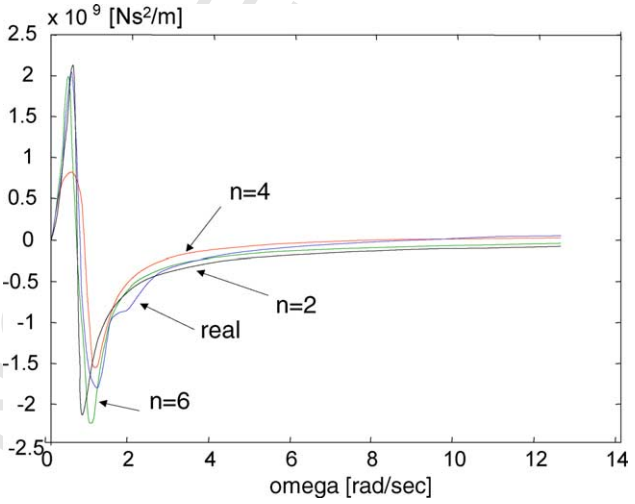

Fig. 34. Optimal estimation of the imaginary part of $h_{15}(j\omega)$ in a spar buoy for different orders.

Table 5
Rational transfer functions for the hydrodynamcis of a spar buoy

$H(s)$	$P_{jk}(s)$ with coefficients: b_4, b_3, b_2, b_1, b_0 $Q_{jk}(s)$ with coefficients: a_4, a_3, a_2, a_1, a_0	γ_{opt}
$P_{11}(s)/Q_{11}(s)$	0, 8.96×10^6, 1.03×10^7, 4.65×10^4, 0 1, 8.44×10^{-1}, -1.06, 2.62×10^{-1}, 1.24×10^{-3}	3.82
$P_{13}(s)/Q_{13}(s)$	0, 8.68×10^6, 9.74×10^6, 3.58×10^4, 0 1, 8.23×10^{-1}, 1.02, 2.52×10^{-1}, 9.70×10^{-4}	3.82
$P_{15}(s)/Q_{15}(s)$	0, 7.50×10^8, 9.06×10^8, 7.11×10^7, 0 1, 8.94×10^{-1}, 1.08, 3.47×10^{-1}, 2.79×10^{-2}	3.60
$P_{33}(s)/Q_{33}(s)$	0, 2.46×10^4, 1.06×10^4, 3.24×10^1, 0 1, 2.76×10^{-1}, 7.65×10^{-2}, 3.33×10^{-3}, 6.54×10^{-10}	2.70
$P_{44}(s)/Q_{44}(s)$	0, 6.14×10^{10}, 6.12×10^{10}, 9.59×10^{10}, 0 1, 7.38×10^{-1}, 2.29, 5.41×10^{-1}, 5.02×10^{-1}	4.05

Table 6
Design parameters for identification of a semisubmersible

n_{jk}	6
m	20
β	0.0001
ω_{c_∞}	1
N_ω	42
p	15
$[\gamma_{min}, \gamma_{max}]$	[0.01, 6]
$[\omega_{min}, \omega_{max}]$	[0.01, 6.5]

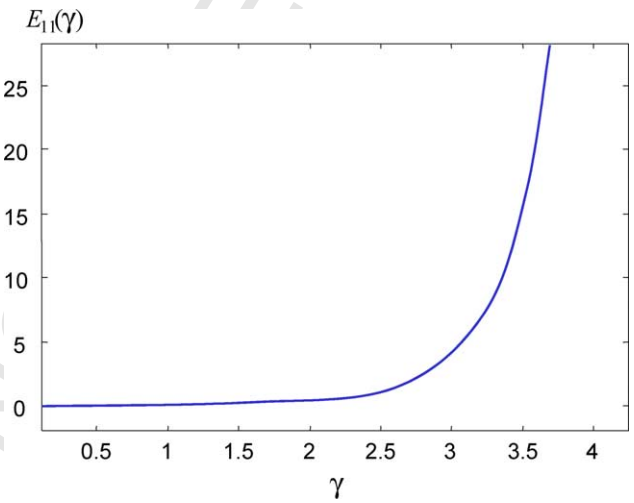

Fig. 35. Course of the weighted LS error along γ in case semisubmersible.

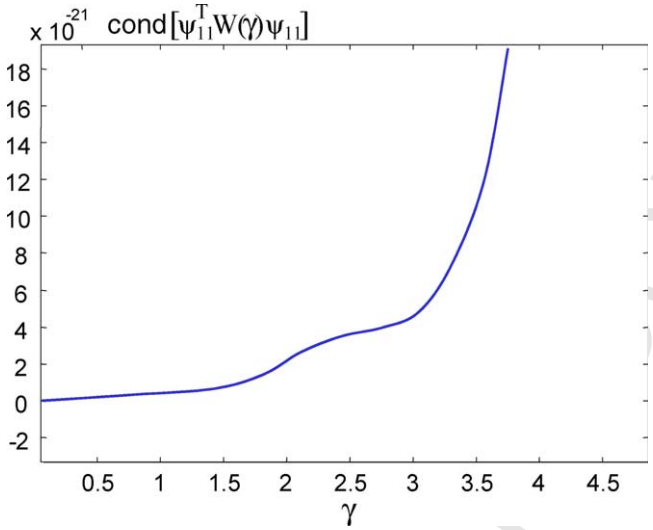

Fig. 36. Course of the condition number of the pseudoinverse along γ in case semisubmersible.

9.3. Case 3: semisubmersible platform

A semisubmersible has generally port/starboard symmetry (i.e., xz-plane of symmetry). Consequently, the complex hydrodynamic matrix is

$$H(\mathrm{j}\omega) = \begin{bmatrix} h_{11} & 0 & h_{13} & 0 & h_{15} & 0 \\ 0 & h_{22} & 0 & h_{24} & 0 & h_{26} \\ h_{13} & 0 & h_{33} & 0 & h_{35} & 0 \\ 0 & h_{24} & 0 & h_{44} & 0 & h_{46} \\ h_{15} & 0 & h_{35} & 0 & h_{55} & 0 \\ 0 & h_{26} & 0 & h_{46} & 0 & h_{66} \end{bmatrix}, \tag{146}$$

with only 12 different elements.

The geometry of the wet hull is complex. Therefore, a reduced-order model is searched for. In Table 6, the design parameters are described for the optimal identification. They remain uniform for all elements h_{jk}.

The constrained optimisation found all stable models with minimum LS error E_{jk} for $\gamma = \gamma_{\min} = 0.01$ as in the case of the spherical buoy (see for example Fig. 35). Also the condition number of the pseudoinverse is best at $\gamma = \gamma_{\min}$ (see for example Fig. 36). Table 7 shows the identified transfer function elements corresponding to the h_{jk}'s on and over the diagonal. Note that $h_{12} = h_{14} = h_{23} = h_{25} = h_{34} = h_{36} = h_{45} = 0$ due to symmetry properties.

The achieved good performance of the approximation with reduced-order models is demonstrated for $d_{11}(\omega)$ and $m_{11}(\omega)$ in Figs. 37 and 38, respectively.

Using the reduced-order model for the hydrodynamics, the behaviour of the semisubmersible (Fig. 9) is simulated in time using the tool AQWA® (AQWA,

Table 7
Rational transfer functions for the hydrodynamics of semisubmersible

$H(s)$	$P_{jk}(s)$ with coefficients : b_6, b_5, b_4, b_3, b_2, b_1, b_0
	$Q_{jk}(s)$ with coefficients: a_6, a_5, a_4, a_3, a_2, a_1, a_0
$P_{11}(s)/Q_{11}(s)$	0, 1.41×10^7, 1.75×10^7, 2.52×10^6, 2.37×10^5, 2.26×10^4, 0
	1, 5.19×10^{-1}, 1.93, 5.38×10^{-1}, 1.57×10^{-1}, 9.85×10^{-3}, 1.29×10^{-3}
$P_{13}(s)/Q_{13}(s)$	0, 1.28×10^7, 1.70×10^7, 2.40×10^6, 2.28×10^5, 2.16×10^4, 0
	1, 5.07×10^{-1}, 1.90, 5.31×10^{-1}, 1.55×10^{-1}, 9.72×10^{-3}, 1.28×10^{-3}
$P_{15}(s)/Q_{15}(s)$	0, 4.32×10^7, 1.91×10^7, 7.64×10^6, -1.29×10^5, 5.65×10^4, 0
	1, 1.76×10^{-1}, 4.67×10^{-1}, 6.22×10^{-2}, 3.21×10^{-2}, 1.79×10^{-3}, 3.27×10^{-4}
$P_{22}(s)/Q_{22}(s)$	0, 3.78×10^7, 1.81×10^7, 1.16×10^7, 8.27×10^5, 1.44×10^5, 0
	1, 4.85×10^{-1}, 1.06, 2.85×10^{-1}, 1.54×10^{-1}, 1.22×10^{-2}, 1.90×10^{-3}
$P_{24}(s)/Q_{24}(s)$	0, 3.78×10^7, 1.81×10^7, 1.16×10^7, 8.27×10^5, 1.44×10^5, 0
	1, 4.8×10^{-1}, 1.06, 2.85×10^{-1}, 1.54×10^{-1}, 1.22×10^{-2}, 1.90×10^{-3}
$P_{26}(s)/Q_{26}(s)$	0, 7.27×10^7, 3.73×10^7, 1.95×10^7, 3.30×10^6, 3.59×10^5, 0
	1, 1.49×10^{-1}, 6.68×10^{-1}, 7.37×10^{-2}, 8.38×10^{-2}, 5.45×10^{-3}, 1.04×10^{-3}
$P_{33}(s)/Q_{33}(s)$	0, 9.87×10^6, 2.93×10^6, 1.69×10^6, 6.77×10^4, 1.49×10^4, 0
	1, 3.79×10^{-1}, 7.52×10^{-1}, 1.32×10^{-1}, 3.18×10^{-2}, 1.63×10^{-3}, 2.35×10^{-4}
$P_{35}(s)/Q_{35}(s)$	0, 9.86×10^6, 2.93×10^6, 1.69×10^6, 6.77×10^4, 1.49×10^4, 0
	1, 3.79×10^{-1}, 7.52×10^{-1}, 1.32×10^{-1}, 3.18×10^{-2}, 1.63×10^{-3}, 2.35×10^{-4}
$P_{44}(s)/Q_{44}(s)$	0, 6.13×10^9, 8.47×10^8, 5.09×10^8, 3.65×10^7, 5.39×10^6, 0
	1, 3.39×10^{-1}, 5.57×10^{-1}, 8.79×10^{-2}, 4.16×10^{-2}, 2.47×10^{-3}, 4.14×10^{-4}
$P_{46}(s)/Q_{46}(s)$	0, 6.13×10^9, 8.46×10^8, 5.09×10^8, 3.65×10^7, 5.39×10^6, 0
	1, 3.39×10^{-1}, 5.57×10^{-1}, 8.79×10^{-2}, 4.17×10^{-2}, 2.47×10^{-3}, 4.14×10^{-4}
$P_{55}(s)/Q_{55}(s)$	0, 8.43×10^9, 3.16×10^9, 1.00×10^9, 5.74×10^7, 9.94×10^6, 0
	1, 3.92×10^{-1}, 7.72×10^{-1}, 1.49×10^{-1}, 5.76×10^{-2}, 3.49×10^{-3}, 5.64×10^{-4}

(continued on next page)

Table 7 (*continued*)

$H(s)$	$P_{jk}(s)$ with coefficients : b_6, b_5, b_4, b_3, b_2, b_1, b_0 $Q_{jk}(s)$ with coefficients: a_6, a_5, a_4, a_3, a_2, a_1, a_0
$P_{66}(s)/Q_{66}(s)$	0, 8.43×10^9, 3.16×10^9, 1.00×10^9, 5.74×10^7, 9.93×10^6, 0 1, 3.92×10^{-1}, 7.72×10^{-1}, 1.49×10^{-1}, 5.76×10^{-2}, 3.49×10^{-3}, 5.64×10^{-4}

2002) for hydrodynamcis analysis in a 3-degree-of-freedom motion (modes: surge, heave and pitch). A monochromatic wave with amplitude and period equal to 1.3 (m) and 13 (s), respectively, excites the platform frontally. Fig. 39 depicts the evolutions of the surge velocity and acceleration of the platform. The evolution of the surge component of the potential-radiation force is shown in Fig. 40. It is seen that the behaviour with reduced-order model follows the true evolution acceptably well both in transitory and stationary state. Similar all-round conclusions are drawn out for the other components of the force in the heave and roll modes.

10. Conclusions

In this paper, a new dynamic model and its parameter identification of the potential-radiation hydrodynamics in moored ocean engineering floating structures like semisubmersibles, barges, buoys and crane-ships are presented. The raw data

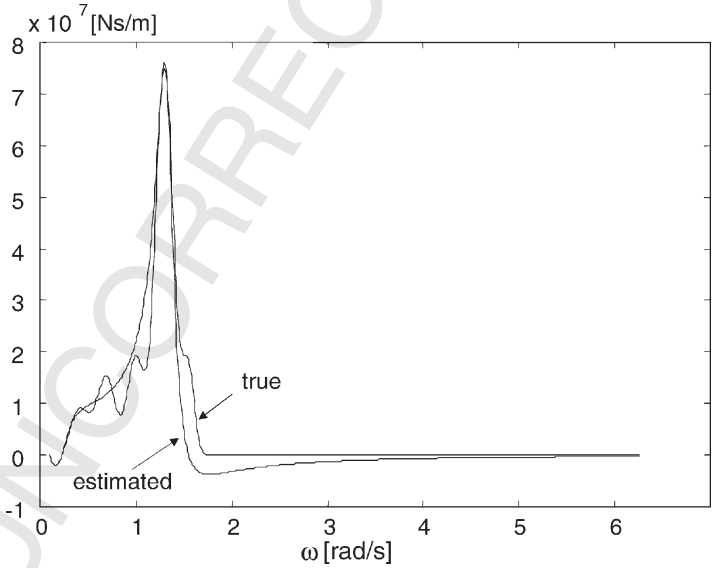

Fig. 37. Optimal estimation of the real part of $h_{11}(j\omega)$ in a semisubmersible.

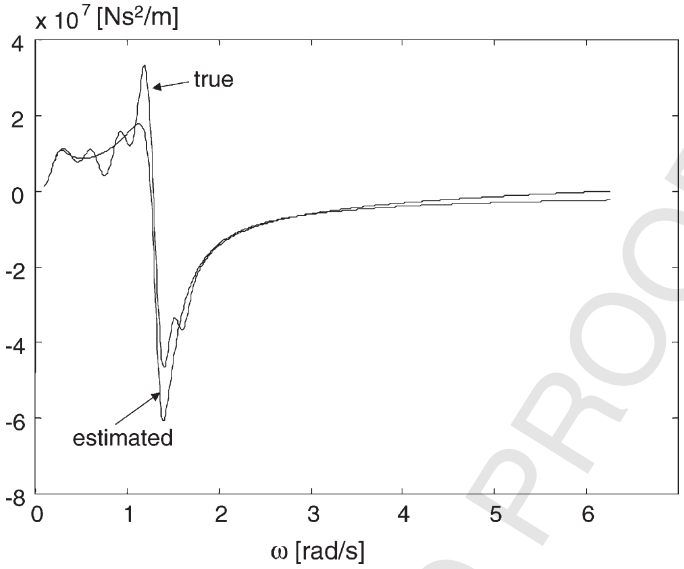

Fig. 38. Optimal estimation of the imaginary part of $h_{11}(j\omega)$ in a semisubmersible.

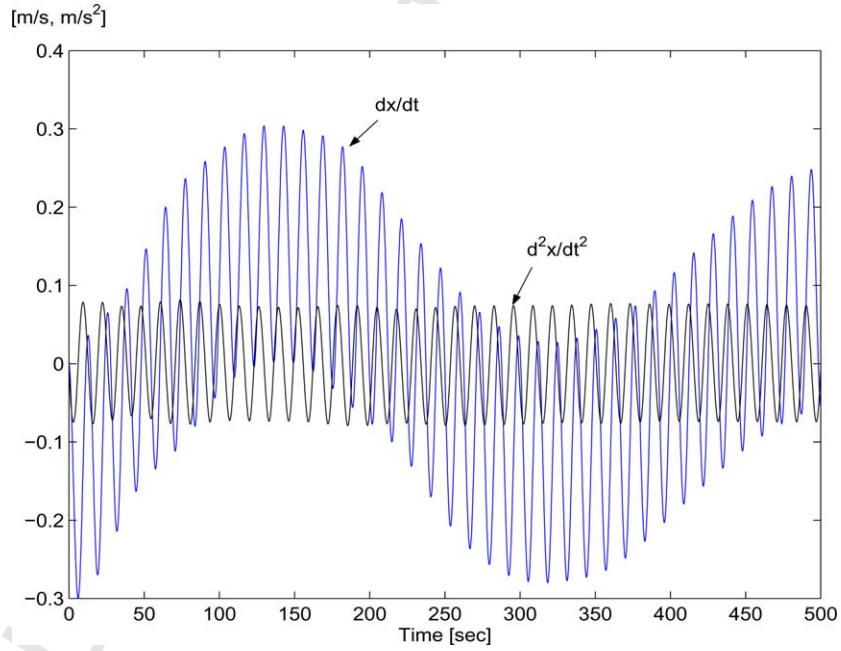

Fig. 39. Evolution of the velocity and acceleration in the surge mode.

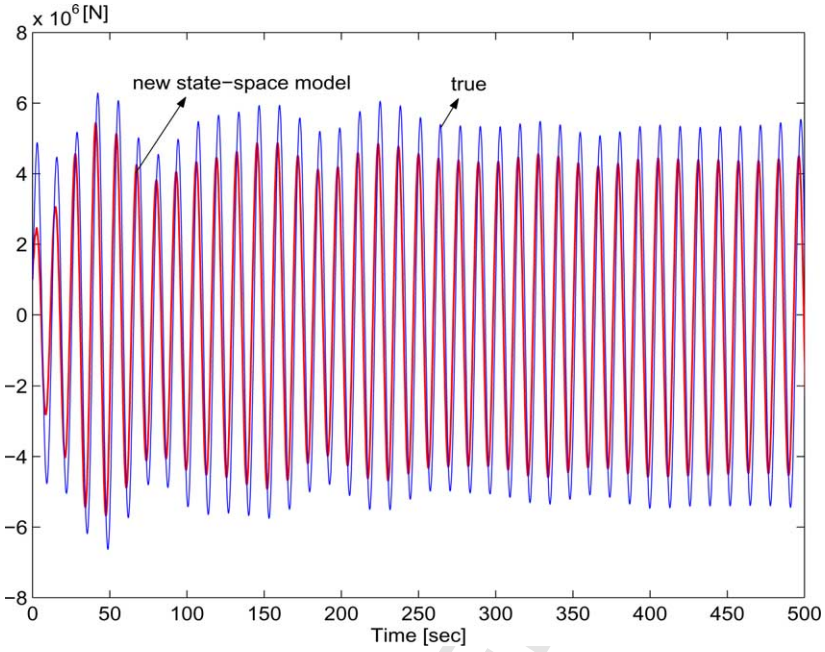

Fig. 40. Evolution of the surge component of the potential-radiation hydrodynamic force.

for these goals are the added-mass and potential-damping matrices in frequency-discrete domain.

In a preliminary study of existing approaches in the literature, two mathematical models and their estimation are comparatively analysed in detail. They are, namely, the convolution model and the state-space model of Jiang (1991). An optimal identification procedure in norm two was developed for the state-space model. One concludes that applications based on the state-space model of Jiang will require low computational costs in comparison with the convolution model. This advantage may be severely shaded by the difficulties in the selection of a suitable approximation order and, still more important, of finding stable models simultaneously. Thus, a state-space model becomes more interesting when an analytical model in the parameters is required. In applications concerning a low or narrow range of frequencies or when the dynamics is only required in stationary state, a state-space model of low order is preferable. On the contrary, when the hydrodynamics is so complex as in semisubmersibles, a large order of approximation is necessary. But in this case, the model stability is so compromised that a convolution model is more beneficial.

In an attempt to share advantages of both approaches, a new state-space model is developed. The identified model possesses a better stability and ensures uniform accuracy for all elements as in the convolution model, but also keeping the analytical and computational benefits of the state-space model of Jiang. The development

is based on the frequency transfer function matrix of the hydrodynamics, whose elements can be characterised by strictly proper rational functions with a single zero at frequency $\omega = 0$. The model is conveniently expressed in the canonical observable form in state space for identification purposes, however, it can be converted into every other usual canonical form.

One important advantage of this model is that the order of every transfer function element can be fitted to data independent of the others. On one side, this leads to a saving in the amount of coefficients in comparison with the state-space representation of Jiang. Additionally, it enables a better control of the stability in over-dimensioned approximations, which may become critical when unstable zero-pole cancellations occur.

The model is identified in a least-squares sense. A weighted norm has to be introduced due to the numerical problems that arise when the regressor columns are of different orders of magnitudes, especially for small and large frequencies. This situation accounts for the ill-conditions of the pseudoinverse. In order to circumvent this numerical instability problem, exponential weighted functions in the frequency and a cost functional of the estimation error in an extended space composed of model parameters and a weighting exponent are developed. A suboptimal solution is encountered by performing an uncoupled double minimization of the cost functional in the extended space. A complete algorithm that accomplishes the tasks of reconstruction in continuous frequency and filtering of the raw data, and finally the parameter estimation upon them are described.

This provides a stable model and reproduces acceptably accurate the behaviour of the potential-radiation hydrodynamic forces in time.

Case studies involving simple and complex geometries of the wet hull of three OE systems serve to demonstrate the features of the proposed approach by numerical simulations.

11. Uncited reference

Sorensen et al. (1999).

12. Acknowledgment

The authors thank Prof. Dr.-Ing. Edwin Kreuzer and Dr.-Ing. Volker Schlegel at the Technical University of Hamburg-Harburg for the theoretical support and test facilities. Dr.-Ing. Mario A. Jordán also thank the CONICET and Scientific Cooperation Project, Germany (AL/A99–EX II/17), for financial support of this investigation.

References

Aamo, M.O., Fossen, T.I., 1999. Controlling line tension in thruster assisted mooring systems. In: IEEE International Conference on Control Applications, pp. 1104–1109.

Aström, K.J., Wittenmark, B., 1996. Computed Controlled Systems: Theory and Design, third ed. Prentice-Hall, New York.

AQWA, 2002. AQWA Reference Manual, Version 5.3A. Century Dynamics Ltd.

Bracewell, R.N., 1978. The Fourier Transform and its Applications. McGraw-Hill, Kogakusha.

Chakrabarti, S.K., 1994. Offshore Structure Modeling. World Scientific Publishing Co. Pte. Ltd, Singapore.

Cummins, W.E., 1962. The impulse response function and ship motions. Schiffstechnik 9 (1), 101–109.

Dean, R.G., Dalrymple, R.A., 1991. Water Wave Mechanics for Engineers and Scientists. World Scientific Pub. Co.

Fajinmi, A.A., Brown, D.T., 1999. Draught control for floating vessels using pneumatics. Engineering Structures 21, 112–124.

Fossen, T.I., 1994. Guidance and Control of Ocean Vehicles. John Wiley & Sons, Chichester.

Gawad, A.F.A., Ragab, S.A., Nayfeh, A.H., Mook, D.T., 2001. Roll stabilization by anti-roll passive tanks. Ocean Engineering 28, 457–469.

Gottlieb, O., Yim, S.C.S., 1997. Nonlinear dynamics of a coupled surge-heave small-body ocean mooring system. Ocean Engineering 24 (5), 479–495.

Guckenheimer, J., Holmes, P., 1997. Nonlinear Oscillations, Dynamical Systems and Bifurcations of Vector Fields. Springer Verlag.

Jiang, T., 1991. Untersuchung nichtlinearer Schiffsdynamik mit Auftreten von Instabiltät und Chaos an Beispielen aus der Offshoretechnik. Technical Report Nr. 512, PhD thesis, Institut für Schiffbau der Universität Hamburg.

Jordán, M.A., Beltán-Aguedo, R., 2003. Optimal identification of hydrodynamics for marine structures and vehicles—two general approaches in time-domain. In: CD-ROM Proceedings of the RPIC03, San Nicolas, Argentina.

Kim, B.K., Bernitsas, M.M., 2001. Nonlinear dynamics and stability of spread mooring with riser. Applied Ocean Research 23 (2), 111–123.

Kreuzer, E., Ellermann, K., Markiewicz, M., 2002. Nonlinear dynamics of floating cranes. Nonlinear Dynamics 27, 107–183.

Landa, P.S., 2001. Regular and Chaotic Oscillations. Springer Verlag, Berlin.

Ogilvie, T.F., 1964. Recent progress toward the understanding and prediction of ship motions. In: Symposium on Naval Hydrodynamic, Washington, DC, pp. 3–128.

Schelin, T.E., Jiang, T., Östergaard, C., 1993. Response analysis and operating limits of crane ships. Journal of Ship Research 37, 225–238.

Sorensen, A., Strand, J.P., Fossen, T.I., 1999. Thruster assisted position mooring system for turret-anchored fpsos. In: IEEE International Conference on Control Applications, pp. 1110–1117.

Soylemez, M., Atlar, M., 2000. A comparative study of two practical methods for estimating the hydrodynamic loads and motions of a semi-submersible. Journal of Offshore Mechanics and Arctic Engineering 122, 57–63.

Umar, A., Datta, T.K., 2003. Nonlinear response of a moored buoy. Ocean Engineering (in press).

Wu, J.S., Hsieh, M., 2001. An experimental method for determining the frequency dependent added mass and added mass moment of inertia for a floating body in heave and pitch motions. Ocean Engineering 28, 417–438.

Youssef, K.S., Ragab, S.A., Nayfeh, A.H., Mook, D.T., 2002. Design of passive anti-roll tanks for roll stabilization in the nonlinear range. Ocean Engineering 29 (2), 177–192.